PRIMER

Muon spin spectroscopy

Adrian D. Hillier[1]✉, *Stephen J. Blundell*[2], *Iain McKenzie*[3,4,5], *Izumi Umegaki*[6], *Lei Shu*[7], *Joseph A. Wright*[8], *Thomas Prokscha*[9], *Fabrice Bert*[10], *Koichiro Shimomura*[11], *Adam Berlie*[1], *Helena Alberto*[12] *and Isao Watanabe*[13]

Abstract | Muons are particles with a spin of ½ that can be implanted into a wide range of condensed matter materials to act as a local probe of the surrounding atomic environment. Measurement of the muon's precession and relaxation provides an insight into how it interacts with its local environment. From this, unique information is obtained about the static and dynamic properties of the material of interest. This has enabled muon spin spectroscopy, more commonly known as muon spin rotation/relaxation/resonance (μSR), to develop into a powerful tool to investigate material properties such as fundamental magnetism, superconductivity and functional materials. Alongside this, μSR may be used to study, for example, energy storage materials, ionic diffusion in potential batteries, the dynamics of soft matter, free radical chemistry, reaction kinetics, semiconductors, advanced manufacturing and cultural artefacts. This Primer is intended as an introductory article and introduces the μSR technique, the typical results obtained and some recent advances across various fields. Data reproducibility and limitations are also discussed, before highlighting promising future developments.

Gyromagnetic ratio
The ratio of a particle's magnetic moment to its angular momentum; for a muon, the gyromagnetic ratio is $2\pi \times 135.5\,\mathrm{MHz\,T^{-1}}$.

Spin-polarized
The degree to which the spins are aligned along a particular direction.

✉e-mail: adrian.hillier@stfc.ac.uk

https://doi.org/10.1038/s43586-021-00089-0

The muon, μ, is a fundamental particle similar to the electron, with an electric charge of $-e$ and a spin of ½, but with greater mass (TABLE 1). Both the mass and the gyromagnetic ratio of the muon are between those of the electron and the proton. In materials, the negative muon (μ^-) behaves similar to a heavy electron and its antiparticle, the positive muon (μ^+), is similar to a light proton. The discovery of the muon is generally attributed to Anderson and Neddermeyer[1] building on the investigations by a Jesuit priest[2] and some adventurous balloon travel[3] whereas the history of muon spin spectroscopy can be traced back to a seminal paper by Garwin et al.[4] and the measurement of the muon lifetime in Rome[5].

Most condensed matter muon spin spectroscopy studies use the positive muon, μ^+. Primarily, this is because, compared with the negative muon, μ^+ has an increased production rate and polarization is maintained during sample implantation. A critical advantage of muons is that the experiment can be conducted in zero field, as the muon is spin-polarized at its source. This means that muons do not require a specific element to be present in the sample. Unlike many other techniques, such as neutron or X-ray scattering and spectroscopy, muons are implanted into the sample and can be considered analogous to nuclear magnetic resonance (NMR) and electron paramagnetic resonance (EPR) as the depolarization of a spin-polarized species is measured. Although other methods, such as X-ray absorption spectroscopy, can be used to study magnetic atoms to investigate the spin and orbital angular momentums, the muon is a much more sensitive probe to weak magnetism. This makes it more appropriate for systems with diffuse moments, for example, to study magnetic materials with short-range order or organic-based systems. Similarly, neutron spectroscopy can be used to study a wide range of both hard and soft matter, across areas from magnetism and ionic diffusion to liquid interfaces and lattice vibrations. However, the time window is different for neutron spectroscopy and neutron scattering is often less sensitive to weak electronic and nuclear moments when compared with muon techniques. On implantation into a sample, positive and negative muons interact with their local environment before decaying into a positron, for μ^+, or an electron, for μ^-. This decay occurs preferentially along or opposite to the final spin direction. By monitoring the spin polarization, information about the material of interest can be obtained. The positively charged muon implants within a interstitial site in the chemical structure, making it sensitive to the physics of the electrons and surrounding nuclei (provided they have a nuclear moment), whereas the negatively charged muon implants close to the atomic nucleus, and can yield information about the identity of the capturing atom and local magnetism.

To produce polarized muons in significant quantities, a proton accelerator is required. These large facilities are often expensive to build and operate. Consequently, they are user facilities that scientists visit. There are currently five sources that produce muons useful for investigating materials, namely, in chronological order: TRIUMF (Canada), PSI (Switzerland), ISIS (UK), J-PARC (Japan)

Author addresses

[1]ISIS Neutron and Muon Facility, STFC Rutherford Appleton Laboratory, Didcot, UK.
[2]Clarendon Laboratory, Department of Physics, University of Oxford, Oxford, UK.
[3]TRIUMF, Vancouver, British Columbia, Canada.
[4]Department of Chemistry, Simon Fraser University, Burnaby, British Columbia, Canada.
[5]Department of Physics and Astronomy, University of Waterloo, Waterloo, Ontario, Canada.
[6]Toyota Central R&D Labs., Inc., Nagakute, Aichi, Japan.
[7]State Key Laboratory of Surface Physics, Department of Physics, Fudan University, Shanghai, China.
[8]School of Chemistry, University of East Anglia, Norwich, UK.
[9]Laboratory for Muon Spin Spectroscopy, Paul Scherrer Institute, Villigen, Switzerland.
[10]Université Paris-Saclay, CNRS, Laboratoire de Physique des Solides, Orsay, France.
[11]High Energy Accelerator Research Organization (KEK), Tsukuba, Ibaraki, Japan.
[12]University of Coimbra, CFisUC, Department of Physics, Coimbra, Portugal.
[13]Advanced Meson Science Laboratory, RIKEN, Saitama, Japan.

Pions
Particles (either positively, neutral or negatively charged) that decay into a muon and muon neutrinos.

Muon neutrinos
Neutrinos that are produced during the decay process of a muon.

Helicity
The projection of the spin of a particle onto the direction of momentum. The helicity is right-handed if the direction of its spin is the same as the direction of its motion, and left-handed if it is opposite.

and MuSIC (Japan). These are well-established user facilities that have a range of instruments that have been optimized for investigating the broad range of science where muon spectroscopy is of value. The basic instrument consists of a source of muons that are transported to the instrument. Upon arrival at the instrument, a trigger signal activates the data acquisition system and the muons enter the material of interest (the sample). After entering the sample, the muons interact with the local environment and decay, emitting a positron (μ^+) or an electron (μ^-). In the case of the negative muon, a muonic X-ray and γ-ray are emitted during the capture process. The material of interest may be held in a sample holder that allows for control over one or more variables, including the temperature, magnetic field and pressure, during the experiment. Detectors are placed around the material, to time stamp any emission. From these detectors, the time evolution of the muon can be determined. The experimental set-up is normally defined by the applied magnetic field; usually a zero field, longitudinal field and transverse field, relative to the initial muon polarization. During a typical muon experiment, the decay asymmetry of the muon ensemble average is measured, reflecting the evolution of the muon spin polarization. It is often the depolarization that is of interest and, although statistics vary on the level of detail required, typically several million events are counted per data point, for example, at each temperature increment.

This article is intended as an introduction to muon spin spectroscopy, more commonly known as muon spin rotation/relaxation/resonance (μSR), for condensed matter.

Table 1 | **Properties of the muon, electron and proton**

Particle	Charge	Spin	Mass (m_e)	Lifetime (τ_μ)	Magnetic moment (μ_p)	Gyromagnetic ratio, $\gamma_\mu/2\pi$ (MHz/T)
Electron	$-e$	½	1	∞	657	2.80×10^4
Muon	$\pm e$	½	207 (or $0.11m_p$)	2.197 μs (μ+); <2.197 μs (μ−, dependent on capturing atom)	3.18	135.5
Proton	$+e$	½	1,836	∞	1	42.6

m_e, mass of the electron; m_p, mass of the proton.

Although each section can be read in isolation, it is recommended that the Primer be read sequentially. Beginning with Experimentation, a detailed explanation is provided of the technique and experimental acquisition; Results discusses how to treat the acquired data and analyse the results; in Applications, current topics using μSR are reported; Reproducibility and data deposition explores data storage at facilities and calibration values for ensuring the results can be reproduced; in Limitations and optimizations, an overview of some of the practical elements for a successful muon experiment is provided; and, finally, Outlook covers new trends and developments. Throughout the Primer, an overview of the μSR technique is given; however, more information and several specialized and detailed books and articles are available in REFS[6–13].

Experimentation

This section provides an overview of instrument design, with the aim of giving the user some fundamental knowledge about muon experimentation. An understanding of the instrumentation can help to determine whether μSR is a suitable tool for investigating a particular system. This knowledge may also assist with writing a research proposal for access to beamtime. However, every facility will typically have instrument scientists in-house who are available to guide and support users through the experimental set-up and the data acquisition process.

There are two types of muon sources: continuous sources and pulsed muon sources. Each have their own strengths and limitations. TRIUMF, PSI and MuSIC are continuous muon sources that have high timing resolution, whereas ISIS and J-PARC are pulsed sources with high data rates and can measure out to 'long' times. In addition to the intrinsic muon source characteristics, each facility has a range of beamlines. TABLE 2 summarizes the characteristics of each source. The details of each beamline type are discussed in this section.

Muon production, sources and beamlines

To produce muons in a large enough quantity to perform an experiment, protons, p, are collided into a target made of light elements such as carbon or beryllium. This results in pions, π, that decay into muons. This process is summarized below, where n represents neutrons:

$$p + p \rightarrow p + n + \pi^+ \quad (1)$$

$$p + n \rightarrow p + p + \pi^- \quad (2)$$

Because current facilities have proton energies between 500 MeV and 3 GeV, this high-energy collision process creates both negatively and positively charged pions. The decay of pions results in muons and muon neutrinos, ν_μ, where:

$$\pi^+ \rightarrow \mu^+ + \nu_\mu \quad (3)$$

$$\pi^- \rightarrow \mu^- + \bar{\nu}_\mu \quad (4)$$

The spin of the pion is zero and the muon neutrino has a definite helicity. Consequently, the surface muons

Nuclear capture
A nucleus of an atom can capture a muon (μ^-) after cascading down the muonic atom energy levels.

Cyclotron
A particle accelerator that operates by accelerating charged particles with static magnetic fields and a high-frequency radio-frequency electric field, generally producing particles quasi-continuously, resulting in a continuous source of muons.

Synchrotron
A particle accelerator that operates by accelerating charged in a closed loop where magnetic fields are used in a specific synchronized timing.

Time resolution
The minimum time interval that can be measured with a specific technique.

Muonium
An atom formed of a positive muon and an electron, analogous to hydrogen, with a very similar electronic structure but only one-ninth of its mass.

Thermalize
A process where a system reaches thermal equilibrium.

Precess
The response of a particle with spin in a magnetic field that is off-axis to the initial polarization. The relative orientation of the particles spin changes in response to the magnetic field, where the precession can be visualized by picturing a spinning gyroscope.

Time-integral measurements
The integrated polarization of the muon is measured as a function of some external parameter, such as the applied magnetic field or the radio-frequency, which are scanned in a series of steps.

Time-differential measurements
Measurements probing how the muon polarization evolves with time.

produced are 100% spin-polarized, whereas decay muons produced from in-flight pion decay have lower polarization.

Both surface and decay muons themselves decay, emitting a positron e^+ or electron e^-, respectively, and two neutrinos, ν. The positron is emitted preferentially along the direction of the muon spin:

$$\mu^+ \rightarrow e^+ + \bar{\nu}_\mu + \nu_e \quad (5)$$

$$\mu^- \rightarrow e^- + \nu_\mu + \bar{\nu}_e \quad (6)$$

Large-scale user facilities can provide two types of muon beamlines: surface muons and decay muons. Surface muons originate from the decay of the pions, which are at rest, from the surface of the target material. They have a relatively low energy (~4 MeV) and momentum (~28 MeV c^{-1}) with a fairly narrow energy distribution and, most importantly, 100% spin polarization. The yield is also fairly high — which is advantageous because only a small fraction of the pions or muons can be collected and transported to experimental areas — but with a large number of polluting positrons and other particles that must be removed before the muons reach the sample. The surface method is used for the production of μ^+ because most of the stopped negative pions undergo nuclear capture before they decay, and therefore almost no surface negative muons escape from the target. However, the large amount of μ^+ produced provides a high flux of muons for μSR experiments.

In decay muon beamlines, high-energy pions are ejected from the target and transported down a beamline so that pion decay occurs in flight, generally when the pions are contained in a superconducting solenoid whose length is comparable with the pion decay length. Typical momenta for these beamlines range from 40 to 120 MeV c^{-1} and are tuned by varying the dipole magnetic fields. An example of this is shown in FIG. 1, where FIG. 1a shows a generic muon beamline layout[14,15]. This allows for the production of high-energy muons, which are important for pressure cell work and other experiments in which higher muon penetration depths are required, and negative muons, where negative pion extraction from the target is required. The production rate for these higher energy muons is generally lower than for surface energy muons, particularly just above the surface energy, and slowly recovers as the momentum is increased (FIG. 1b).

The proton source generally comes from two different set-ups, a cyclotron or a synchrotron, which are quasi-continuous (23–50 MHz) or pulsed (25–50 Hz), respectively.

A quasi-continuous source uses a cyclotron (PSI in Switzerland, TRIUMF in Canada and MuSIC in Japan[16]), and generates an extremely high flux of muons, in the order of 10^8 mA^{-1} s^{-1}. An advantage of using a continuous source is that the time resolution can be extremely high, and one can measure large frequencies up to, and perhaps beyond, 5 GHz. This enables high muon precession frequencies to be measured, such as those arising from internal fields in magnetic samples and in muonium studies. However, the rate for time-differential measurements is limited by only being able to have one muon in the sample at a time, counting approximately 20 million muons per hour.

Table 2 | **A summary of the facilities and the different beamlines that are available**

Facility	Type of beamline	Momentum (MeV c^{-1})
TRIUMF	Surface	29.5 ± 10%
	Decay	40–120
PSI	Low-energy muons	0.45–2.5
	Surface	28
	Decay	60–125
ISIS	Surface	29
	Decay	15–120
J-PARC	Low-energy muons (in development)	To be confirmed as system is under development
	Surface	30
	Decay	5–120
MuSIC	Surface	28
	Decay	28–80

The technical details of the different muon beamlines are described in Experimentation.

For a pulsed source (ISIS in the UK[15] and J-PARC in Japan[17]), a synchrotron is used to create a pulse of protons with a finite pulse width that collides with a target. The muons produced from the collision travel in bunches with a finite pulse width; at ISIS, this pulse width is approximately 55 ns (REF.[18]) and at J-PARC the pulse width is 100 ns. As the front of the pulse first arrives, the initial muons will thermalize and begin to precess and respond to any local fields before the rest of the muon ensemble arrives. The result of this pulse width is that the time resolution is significantly limited with measurable frequencies up to ~10 MHz. The advantage of the pulse structure is that one has periods of quiet between the pulses, which means the background of the measurement is low and positrons can be recorded for many muon lifetimes (>12τ_μ, 26 μs). Pulsed measurements lead to very high instantaneous data rates — the positrons are detected in the detector system — that require large arrays of positron detectors to cope. This leads to the need to build extensive beamlines and instruments such as those seen at ISIS[15,19] and J-PARC[17]. Another advantage of pulsed muons is the ease with which they can be combined with pulsed extreme conditions such as lasers, a pulsed radio-frequency field, a pulsed electric field, a pulsed current, in situ battery decay and, in principle, pulsed high magnetic fields. This enables both stimulation of the sample and measurement of the physical effects of muon interactions.

In time-integral measurements, there are no restrictions on the number of muons in the sample at one time. As a result, it is possible to run at much higher incident muon rates at a continuous source, far greater than at a pulsed source. Instead, at pulsed source facilities, time-differential measurements and time-integral measurements can be performed simultaneously; however,

continuous source facilities allow for a much higher data rate during time-integral measurements. This higher data rate enables more sensitive measurements. Depending on the research question and information needed, either time-differential or time-integral measurements are optimal.

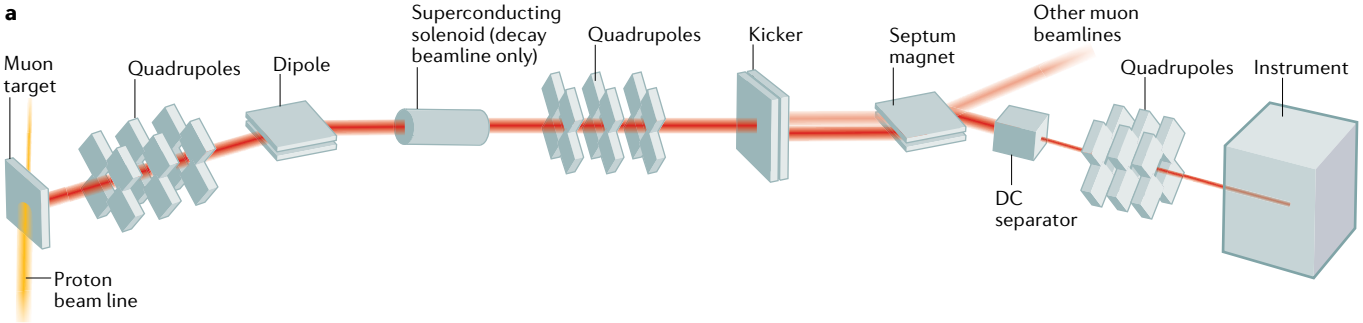

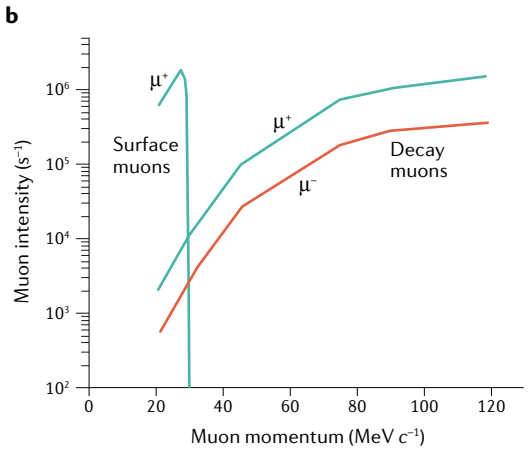

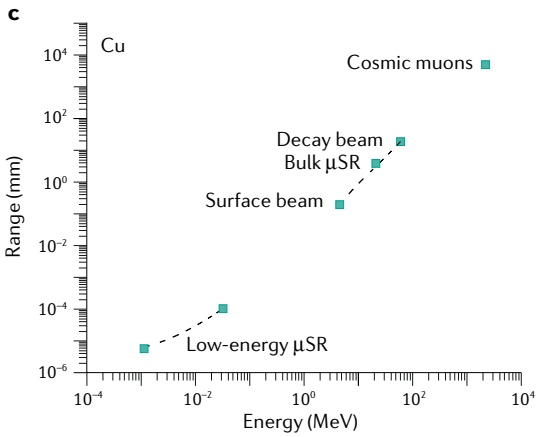

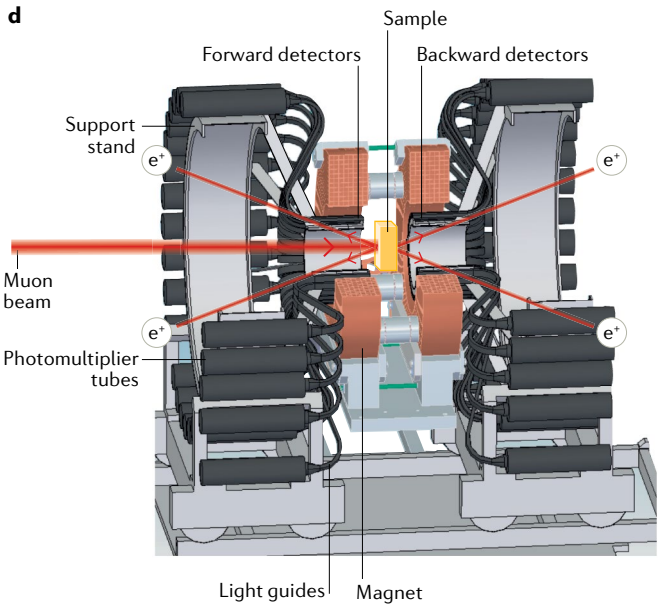

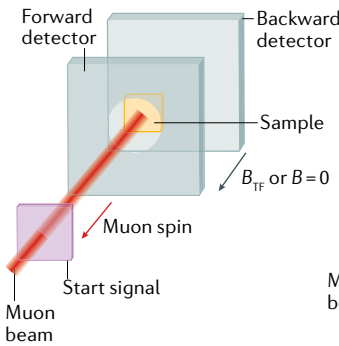

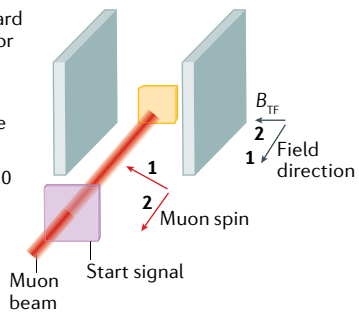

Fig. 1 | **Muon beamlines. a** | General schematic of a muon beamline. **b** | An example of the muon production rate as a function of the muon momentum. These are the muon production rates for the RIKEN-RAL beamlines at ISIS. **c** | Range of muons in copper as a function of muon energy. **d** | Schematic of muon spin rotation/relaxation/resonance (μSR) spectrometer. Number of positrons generated by decay of muons at rest in a sample (yellow) measured using counters placed in front of and behind the sample. Brown segment represents a Helmholtz coil that produces magnetic fields. **e**,**f** | Schematic of a typical muon spin spectrometer in both the longitudinal set-up (part **e**) and the transverse set-up (part **f**). Transverse set-up has two configurations, **1** or **2**, and is instrument dependent. Detectors are pale blue and start detector is pale purple. Start detector may be a muon detector (continuous) or a signal from the accelerator (pulsed). Muon spin is represented by red arrows and field direction by purple arrows. *B*, applied magnetic field; B_{TF}, transverse magnetic field; μ^-, negative muon; μ^+, positive muon. Part **b** adapted with permission from REF.[14], Elsevier.

Box 1 | **Low-energy muon production**

Two-photon ionization of thermal muonium in a vacuum is only possible at pulsed accelerators. Here, a pulsed laser system provides the required laser energy for efficient ionization of muonium, leaving an ultra-slow muon with an energy of about 0.2 eV. At J-PARC, the Ultra-Slow Muon (USM) beamline[203–205] is under development, and consists of a pulsed surface muon beam at 25 Hz that impinges on a 2,000 K hot tungsten foil. From this, a pulsed beam of thermal muonium atoms escapes into vacuum. The ionization of muonium then takes place in two steps: one laser generates Lyman-α photons at 122 nm to excite the 1s–2p transition, and a second laser at 355 nm ionizes the excited muonium atoms.

At continuous and pulsed muon beam facilities, a moderation technique based on cryogenic thin layers of van der Waals bound solids, such as rare gases and nitrogen, significantly reduces the energy of the surface muons to 10–20 eV. In contrast to the laser ionization method, where 50% of the muon polarization is lost in the initial muonium state, the muon polarization is conserved in the moderation process. The most efficient moderators are solid neon and solid argon layers. The Low-Energy Muons Group (LEM) facility at PSI routinely provides up to 2×10^4 $\mu^+ s^{-1}$. In 2006, the LEM opened as a user facility with a user programme for μSR applications on nanometre-thin layers (low-energy μSR)[206,207].

Beamlines are used to transport muons from the target to the sample; the muon then decays and the resulting product is detected. Because muons have both charge and spin, various magnets guide, steer and focus the beam from injection from the target to individual instruments (FIG. 1a). Quadrupole magnets are used to focus the muon beam, where each quadrupole is responsible for focusing along either the *x* or *y* axes and they act together as a series of lenses. When using only quadrupoles, other particles are also transported down the beamline. It is possible to selectively remove these other particles using dipole bending magnets, which also serve to curve the beam to meet the spatial requirements of the beamline. Momentum slits can filter out all particles that do not have the same momentum and charge as the muon, whereas a separator filters out positron contamination — positrons that have the same momentum as the muons but a different velocity — by only letting muons of the desired velocity through. At a pulse source, the proton pulses arrive in two bunches close together (at ISIS, ~300 ns apart). Having both pulses enter a single muon instrument can be detrimental to the frequency response. To maximize the two pulses, the muon beam can be kicked to different individual beamlines, thus enabling two instruments to operate simultaneously. Kickers have also been used at continuous sources to reduce the detector background, giving the instruments a muon on request option[20]. Although bending the path of a muon may also cause a slight rotation to its spin, larger rotations can be achieved by using magnetic fields where the spin of the muon can be rotated between 70° and 90° and an electric cross-field that ensures the muons do not deviate from the beamline. This enables high transverse fields to be measured, which would otherwise send the beam out of the spectrometer.

Quadrupole magnets
Magnets with four pole pieces, generally used in doublets or triplets for focusing of a charged particle beam.

Momentum slits
Slits that allow particles through with a particular momentum, often used in conjunction with a separator to ensure that only muons enter the instruments.

Separator
Two electrically charged plates and a dipole magnet with tuned electric and magnetic fields to act as a Wein filter. Often used in conjunction with momentum slits to ensure that only muons enter the instruments.

Kicked
When a muon or pulse of muons is sent down different beamlines by using either a magnetic or electrostatic force kicking the particles by a determined angle.

Lorentz force
A force on a point charge from a combination of both electric and magnetic fields.

Larmor radius
The radius of the track of a charged particle in a magnetic field.

Muon instrumentation

Muon spin spectrometers. All μSR spectrometers share several common features. First, there is either a muon detector or a pulse that defines the implantation of the muons into the sample. Second, an external magnetic field can be applied either parallel (longitudinal) or perpendicular (transverse) to the initial muon polarization. Alternatively, compensation coils can be used to produce zero magnetic field at the sample. Third, positron detectors are arranged, ideally symmetrically, around the sample in order to reconstruct the time and spatial dependence of the muon spins inside the sample and, hence, the magnitude and fluctuation rate of the local magnetic field.

Muons are produced with their spins antiparallel (surface muons) or parallel (decay muons) to their momentum. Applying a magnetic field transverse to muons with this spin orientation will lead to a deflection of the muon beam due to the Lorentz force and limits the measurements to magnetic fields of less than ~25 mT, otherwise the muon would miss the sample. A longitudinal magnetic field in this geometry does not deflect the muon beam, meaning measurements can be made in magnetic fields of several Tesla, as shown in FIG. 1e. Measurements in transverse magnetic fields up to ~10 T can be performed by applying a magnetic field along the initial muon momentum and rotating the muon spin perpendicular to its momentum prior to implantation, as shown in FIG. 1f. The upper limit of the magnetic field is due to the positron Larmor radius becoming so small that the positrons cannot reach the detectors. The addition of a magnetic field can allow either the magnetic state of the sample to be changed or decouple the muon from a particular magnetic environment. In complicated situations, both may occur.

The muon polarization is proportional to the asymmetry in the numbers of positrons detected in opposing pairs of detectors. The configuration of the positron detectors depends on whether the measurement is conducted in a transverse field or longitudinal field, and whether the orientation of the muon spin prior to implantation can be manipulated. Some μSR spectrometers are optimized for either high transverse field or longitudinal field experiments, whereas others can be used for both types of measurement.

Low-energy muons. Muons originating from pion decay have a kinetic energy of about 4.2 MeV. The penetration depth of muons with energies in the mega-electronvolt range in solid matter is from submillimetres to centimetres (FIG. 1c). With these muons, the application of μSR is limited to studies of bulk materials. To extend μSR to nanometre-thin layers such as thin films, heterostructures or near-surface regions, low-energy muons (BOX 1) with energies in the kilo-electronvolt range are required. Two techniques are currently being explored for this purpose[21]: two-photon ionization of thermal muonium, and a moderation technique based on cryogenic thin layers of van der Waals bound solids. Both require surface muon beams with high intensities ($>10^8$ $\mu^+ s^{-1}$) to convert a small fraction ($\leq 10^{-4}$) of the incoming beam into ultra-slow muons, with energies in the range of 0.2–20 eV. Post-acceleration by electrostatic fields then tunes the beam energy in the range of ≤1 keV to 30 keV.

External stimulation. In the standard muon spectrometer, the sample is enclosed in a cryostat or furnace and the instrument has a fixed magnet that can deliver

a fixed range of fields. This enables the sample to be exposed to a range of temperatures, from ~20 mK to 2,000 K. By using thin cryostat or furnace windows — typically made from Mylar, aluminium or titanium — it is relatively easy for muons to enter a sample. In addition, other stimuli can be applied, including but not limited to, pressure, radio-frequency, light and electric field. However, the need to inject muons through the wall of a pressure cell, plus the size of the muon beam within a sample volume, limits the applied pressure to ~2.8 GPa (REFS[22,23]) using current technology.

Radio-frequency μSR is complementary to the NMR technique. The radio-frequency firing timing can be controlled to either synchronize with the injection of the muons or to occur later at a predetermined time. The time dependence of fast changes in the electronic state is sensed within the μSR time range up to about 15 μs. The muon spin rotates during application of radio-frequency in applied longitudinal fields. This technique can be applied to measure the transverse muon spin rotation in strong longitudinal fields[24], to monitor the decoupling of specific nuclei, in pulse techniques[25] and for measuring reaction rate constants[26]. A recent development is the ability to stimulate a sample with photon irradiation. Early studies used flash lamps, whereas newer work uses laser technology[27–29]. Another technique applies electric fields to manipulate the properties of the sample and investigate charge dynamics[30].

Elemental analysis

To use muons for elemental analysis, negatively charged muons are required. Using negative muons, muonic X-rays are emitted and their energies are dependent on the capturing atom. When a negative muon is implanted into the sample, it is readily captured by an atom in the material, to form a muonic atom, with a capture probability approximately proportional to the atomic number Z and at an energy level of $\sim n \sim 14$. Initially, the muon ejects Auger electrons that are usually self-absorbed and not observed. After forming the muonic atom, the muon cascades down to the lowest energy level, $n = 1$. During each cascade, the muon emits an X-ray and, given that the mass of the muon is ~200 times that of an electron, these X-ray emissions range from tens of kilo-electronvolts to 8,000 keV. The energy resolution is determined by the detector technology, for example, high-purity germanium, and varies as a function of energy from ~ 0.5 keV at low energy to 5 keV at high energy. The Kα energies are shown in FIG. 2a and an example of a muon cascade in FIG. 2b. These high energies allow for observation of elements from lithium up to the highest Z value. Although lighter elements, such as helium and hydrogen, can be observed, the low-energy muonic X-rays make self-absorption effects problematic. The main advantage of using muons for elemental analysis over other techniques is that it is non-destructive, is sensitive to all elements (including light elements), can measure deep within the sample and not just the surface composition, can be used for depth profiling from tens of nanometres to centimetres and does not make the samples active (FIG. 2c,d). This has resulted in the technique becoming highly attractive for areas including cultural heritage, advanced manufacturing, energy materials and biosystems.

These instruments require decay channel muon beamlines and there are currently two muon facilities that are running user programmes, ISIS and J-PARC, whereas the facilities at PSI, TRIUMF and MuSIC are developing this technique. The experimental set-ups are quite similar; they consist of numerous high-purity germanium detectors arranged around the sample, with a range of energy efficiencies and resolution. The notable difference between the ISIS and J-PARC set-up is the vacuum chamber at the sample position at J-PARC. This enables a reduced background at the lowest incident muon momenta.

The time relative to the muon implantation and energy of the X-ray emissions is determined. As the momentum of the negative muon beam is known, these measurements can be depth-resolved[31,32], enabling a compositional analysis as a function of depth. Recent developments use highly pixelated areas to directly image the sample under investigation. One approach is to place the detector as close as possible to the sample[33], but, alternatively, a pinhole camera may be used instead[34].

Sample mounting

How a sample is mounted can be the difference between a successful and an unsuccessful experiment. Consequently, sample mounting should be considered before the experiment starts. Although there are differences between facilities, the same principles apply.

Generally, a sample holder should be used that minimizes relaxation of the muon polarization. Normally, elements with small nuclear moments, μ_N, are used. Examples of these are detailed in TABLE 3. However, some elements with large μ_N may be used because they are cheap and easy to machine. If these elements are used as a holder, a correction needs to be added to the data for muons that stop in these materials rather than in the sample. Many different sample holders exist across the different facilities. Commonplace holders include gluing the sample onto a silver backing plate on the cooling stage of the cryostat; creating a silver foil packet; larger squares of aluminium, silver or titanium with shapes milled out for powders to sit within; or more specialist equipment. For sub-0.3 K measurements, small amounts of dilute GE varnish, a standard varnish with good thermal properties, can be poured on powder samples to help thermal conductivity.

Other, more exotic methods for containing or mounting examples are available, for example, cells may be used for air-sensitive samples and liquids, which require the same considerations previously discussed. Large sample cells exist for gaseous samples, where a large amount of gas is needed to stop the muons. Experiments studying muonium or muoniated radicals in liquids and gases require oxygen be removed before encapsulation as oxygen can react rapidly with these paramagnetic species. Oxygen can be removed by repeated cycles of freeze–pump–thawing or by bubbling with argon for an extended period. Lastly, pressure cells have been developed at different facilities[22,23]. These often require large amounts of sample and the pressure medium can

Muonic atom
A negative muon captured and bound to an atom.

Auger electrons
Auger electrons result from the response of an atomic shell with a core vacancy induced by an external (electron or photon) excitation. An Auger electron released from the outer shell of the excited atom while another outer shell electron relaxes to the core vacancy.

Kα energies
The energy of an X-ray emitted when undergoing a transition between the 2p and 1s atomic energy levels

either be through an oil or gas. In these circumstances, the cell itself may have a muon relaxation rate that is temperature-dependent.

Results

This section discusses different ways to reduce and analyse data for the range of experimental set-ups, from time differential in both longitudinal and transverse geometries; to avoided level crossing muon spin spectroscopy and elemental analysis; along with some standard software packages. More detailed description can be found in the standard textbooks[6–8,11].

Muon implantation

The first step of a μSR experiment is implantation of muons into the material of interest. The muon enters the sample with a relatively high energy, typically between 4 and 40 MeV. The muon rapidly thermalizes in the sample. The initial stages reduce the muon energy to 2–30 keV, through ionization of the atoms and scattering with electrons ($\Delta t \sim 10^{-9}$ s). Next, formation of muonium occurs as a result of successive electron capture and loss ($\Delta t \sim 10^{-13}$ s). During this process, the energy of the muon is further reduced to ~50 eV. Finally, the muonium atom collides with atoms and thermalized muonium dissociates, yielding a thermalized muon. Once in a thermalized state, the muon is a free muon (in a diamagnetic state), meaning it localizes at an interstitial site in the crystal structure, or picks up an electron to form muonium (a paramagnetic state, Mu). In this state, the muon can be considered as a light isotope of hydrogen and is chemically very similar: Bohr radius $a_{Mu} = 1.004 a_H$ and ionization potential $I_{Mu} = 0.996 I_H$, but with a reduced mass, $m_{Mu} = 1/9 m_H$. The final possible state is a muoniated radical (a paramagnetic state) where the muon is chemically bound in a molecule containing an unpaired electron. The state that muon forms depends on the sample under investigation. By forming these variable states, different information can be obtained. For example, for most metallic and/or magnetic systems a 'free' muon is found, for some semiconductors and insulators muonium can be formed, and for systems that have

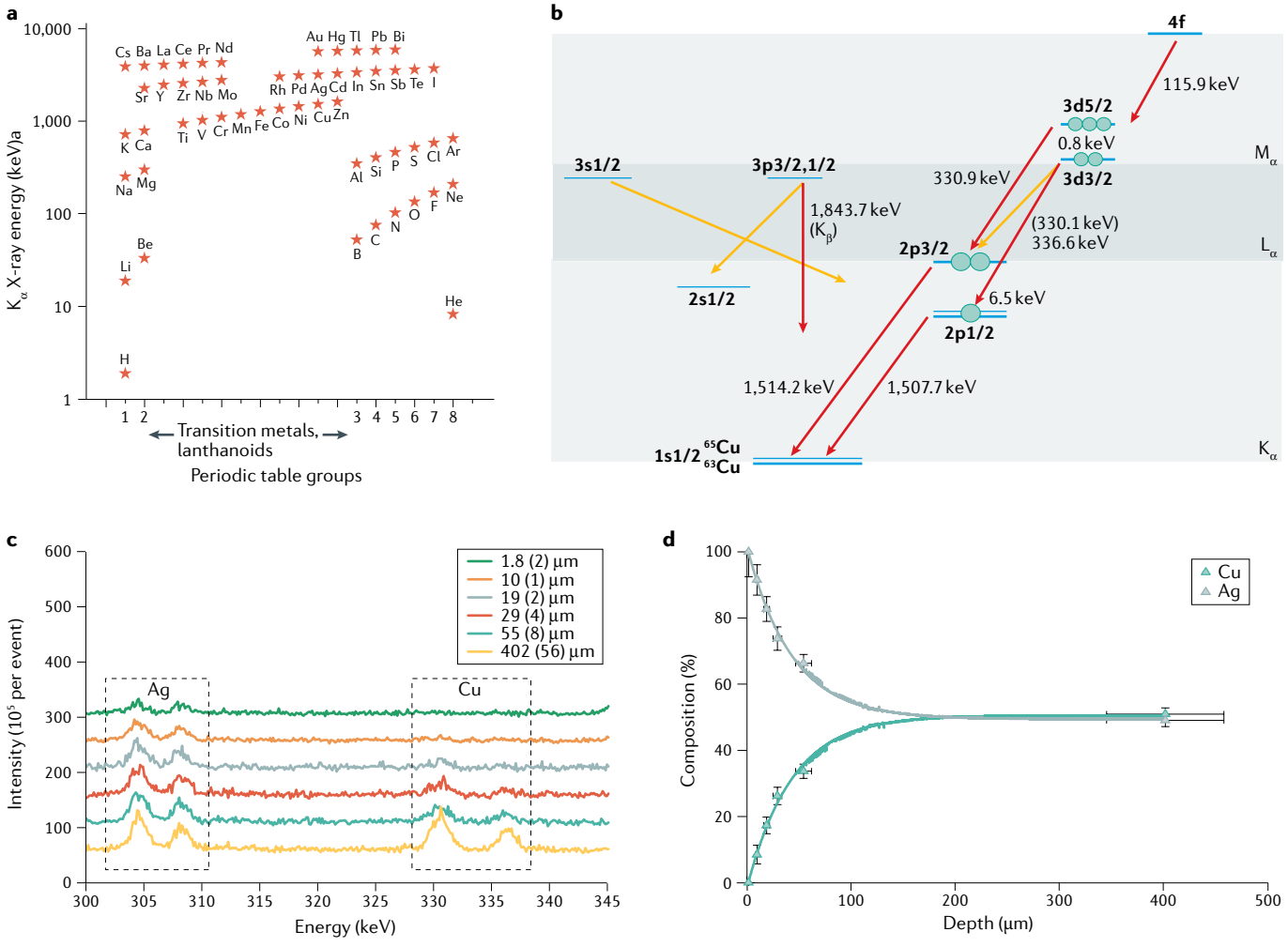

Fig. 2 | **Elemental emission of muonic X-rays. a** | Muonic K_α emission energies for stable elements in the periodic table. **b** | Muon cascade after initial capture showing possible emission spectra from copper. K_α, L_α and M_α transitions are from electron shell $n = 2$ to 1, $n = 3$ to 2 and $n = 4$ to 3, respectively. **c** | Momentum dependence of silver and copper muonic X-ray peaks in the energy range 300–345 keV. Momentum/depth is highest for bottom spectrum (yellow) and lowest for top spectrum (green). This shows absence of copper at the lowest momentum/depth, therefore near the surface of the sample. **d** | Depth dependence of the elemental composition of the data in panel **c**. Parts **c** and **d** are adapted from REF.[165], CC BY 4.0 (https://creativecommons.org/licenses/by/4.0/).

Table 3 | **Common elements used to make sample holders**

Element/isotope	Abundance (%)	*I*	μ (μ_N)
^{107}Ag	51.8	1/2	–0.114
^{109}Ag	48.2	1/2	–0.131
^{47}Ti	7.4	5/2	–0.788
^{48}Ti	73.7	0	0
^{49}Ti	5.41	7/2	–1.104
^{27}Al	100	5/2	3.641
^{63}Cu	69.2	3/2	2.223
^{65}Cu	30.8	3/2	2.382
^{1}H (plastics)	~100	1/2	2.793
^{56}Fe (stainless steel)	91.8	0	0
^{52}Cr	83.8	0	0
^{53}Cr	9.6	3/2	–0.475

Nuclear moment of their main isotopes are shown. *I*, nuclear spin; μ_N, nuclear moment of the isotope.

unsaturated bonds a muoniated radical may form. The state of the muon can change on the timescale of the μSR experiment. In all cases, the muon will interact with its local environment and the muon will decay into a positron or electron (μ^+ or μ^-) preferentially along or opposite to the final spin direction. By monitoring the polarization, information about the material of interest can be obtained.

Time-differential muon spectroscopy

At any given time, there is usually only one muon in a sample at a continuous facility and up to a few thousand muons in a volume of ~0.5 cm^3 at a pulsed facility. Consequently, muon–muon spin interactions in the sample do not need to be considered. The spin precession of the muon can be studied by measuring the positron or electron emitted after μ–e decay. The detectors are constructed with a fast scintillating material, light guide and photomultiplier tube or silicon photomultiplier. From this, light is converted into a time-stamped electrical signal, often with picosecond timing. When applying the μSR method to various materials, whether with continuous or pulsed muons, the time-differential method is the most commonly used approach.

If a positive muon is implanted into a sample and rests at an intermediate position in the crystal structure, it decays into a positron and two neutrinos with a mean lifetime of 2.2 μs (data from NIST). In principle, the muon spin is 100% polarized and the positron is emitted preferentially in the spin direction, with an angular distribution, $W(\theta) = 1 + A\cos\theta$, where θ is the angle between the muon spin and the direction of positron emission, and A is energy-dependent, approximately 0.3 on average.

Time-differential μSR can be classified into three types of measurements depending on the presence or absence of an external magnetic field and its direction: zero field, longitudinal field and transverse field. In zero field measurements, no external field (less than 5 μT) is applied. By taking advantage of the 100% polarization of muons, the zero field measurement is a unique method to find antiferromagnetism, which is difficult to observe by macroscopic methods. In addition, the volume fraction of any magnetic transition can also be measured. During longitudinal field measurement, an external field is applied parallel to the initial muon polarization. By measuring at different external magnetic field values, it is possible to obtain rough values of the internal magnetic field distribution or dynamics, or the hyperfine structure of muonium formed in the material. The muon spin relaxation rate provides information about dynamic processes in the sample. Finally, transverse field measurements apply an external field perpendicular to the initial muon polarization. The muon spin precesses around the total field at the muon site.

A diagram of a μSR spectrometer is shown in FIG. 1d–f. The red line indicates the muon that arrives from the left side and rests in the sample, with spin antiparallel to the momentum (surface muons). The detectors are placed before (forward) and after (backward) the sample.

For zero field and longitudinal field experiments, the time evolution of the positron, $N(t)$, count can be expressed by the following equation:

$$N(t) = N_0 \exp\left(-\frac{t}{\tau_\mu}\right)(1 + a_0 P_z(t)) \quad (7)$$

where $P_z(t)$ is the polarization function, which is 100% polarized (for μ^+) at $t = 0$, and changes with time depending on the interaction with the sample; τ_μ is the muon mean lifetime, and the a_0 term is the empirical maximum from the spectrometer (see FIG. 3a for an example of the positron counts as a function of time). The polarization $P_z(t)$ is equivalent to the longitudinal relaxation function, $G_z(t)$. In order to determine $P_z(t)$ or $G_z(t)$ the counts in the forward and backward detectors are summed (N_F and N_B, respectively) and evaluated by:

$$a_0 P(t) = a_0 G_z(t) = \frac{N_F(t) - \alpha N_B(t)}{N_F(t) + \alpha N_B(t)} \quad (8)$$

where α is a calibration constant (FIG. 3b). By analysing this expression, information about the interaction with the sample at the muon site can be obtained. Common functional forms for $G_z(t)$ are the Kubo–Toyabe function[35], a damped cosine, an exponential decay and combinations thereof[5,8,11,13].

For transverse field experiments, the polarization function becomes (sometimes multiple terms have to be summed):

$$P_x(t) = G_x(t)\cos(\gamma_\mu B_{TF} t) \quad (9)$$

where γ_μ is the gyromagnetic ratio of the muon and B_{TF} is the transverse magnetic field. The functional form of $G_x(t)$ and changes to B_{TF} yield information on the sample under investigation. This is commonly used in Knight-shift measurements and superconductivity. If oscillations are observed in either longitudinal or transverse experiments, further analysis can be useful, for example, Fourier transforms or maximum entropy techniques[36].

Hyperfine structure
A small shift and/or splitting of the energy levels caused by interactions between the nucleus and the electron clouds, known as hyperfine interactions.

Longitudinal relaxation
The depolarization of the muon spin along the longitudinal or *z* direction, parallel to the initial muon spin.

Muoniated radicals
Radicals are molecules with an unpaired electron. Muoniated radicals contain a covalently bound Mu and are formed by Mu addition to an unsaturated bond.

Muon hyperfine coupling constant
The strength of interaction between the magnetic moments of the muon and an unpaired electron.

Nuclear hyperfine coupling constants
The strengths of interaction between the magnetic moments of a nucleus and an unpaired electron. They only occur for nuclei with non-zero spin.

Avoided level crossing muon spectroscopy

Avoided level crossing muon resonance (ALC-μSR) is used to characterize muoniated radicals by measuring the muon hyperfine coupling constant in the solid state and nuclear hyperfine coupling constants. Measuring the muon and nuclear hyperfine coupling constants enables mapping of the distribution of the unpaired electron, which can be used to identify the structure and conformation of radicals[37]. The more hyperfine coupling constants measured, the more that can be determined about the structure of the radical.

Muon asymmetry is determined by integrating the counts in the forward and backward detectors. At specific values of the applied field — which depends on the value of the hyperfine coupling constants — nearly degenerate spin state pairs are mixed by hyperfine interaction. As a result, the muon polarization oscillates between the two mixing states causing a resonant-like change in the asymmetry as the magnetic field varies. Two types of resonance are often observed, characterized by the selection rule $|\Delta M| = 0$ and 1, where M is the sum of the quantum numbers for the z components of the muon and nuclear spins. Commonly, the shorthand notations Δ_0 and Δ_1 resonances are used, respectively.

Δ_0 resonances are observed for muoniated radicals in solids, liquids or gases. The resonance field for a Δ_0 resonance is given by:

$$B_{\mathrm{res}}^{\Delta_0} = \frac{1}{2}\left[\frac{A_\mu - A_X}{\gamma_\mu - \gamma_X} - \frac{A_\mu + A_X}{\gamma_e}\right] \quad (10)$$

where A_μ is the muon hyperfine coupling constant, A_x is the nuclear hyperfine coupling constant and γ_x is the nuclear gyromagnetic ratio[38]. The nucleus X could be

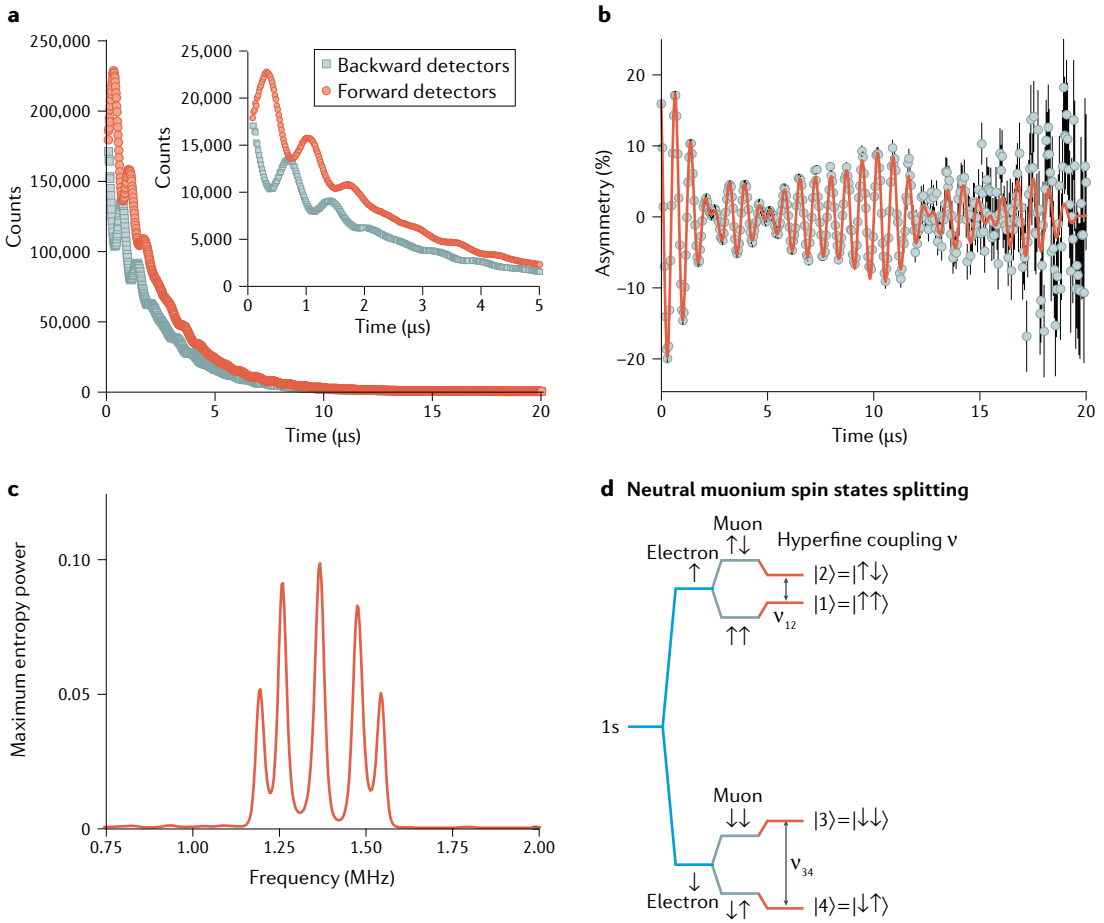

Fig. 3 | **Muon spin spectroscopy (μSR) of CdS. a** | Positron counts as a function of time, summed into forward and backward detectors. **b** | Muon spin rotation (μSR) time spectrum for undoped CdS single crystal at 4.1 K, under an external magnetic field of $B = 0.01$ T. Field direction is perpendicular to the muon spin and parallel to the hexagonal <0001> axis of the sample. **c** | Fourier maximum entropy transforms of the time spectrum in part **b**[36]. Central line represents Larmor precession frequency of the Mu^+ charge state, whereas two additional line pairs are associated with a weak muon–electron bound state and a neutral Mu^0 in a shallow defect centre. Muonium lines arise from transitions between hyperfine energy levels of Mu^0 spin states in the high-field limit, consistent with a hyperfine tensor with axial symmetry along the Cd–S bond direction[133]. **d** | Splitting of Mu^0 spin states in the high-field limit, illustrating contributions of electron Zeeman energy (blue), muon Zeeman energy (blue–green) and hyperfine coupling between the muon and the electron (red). ↑ and ↓ signs indicate spin up and down, respectively. Each pair of muonium lines observed in parts **b** and **c** correspond to state transitions $|1\rangle \leftrightarrow |2\rangle$ and $|3\rangle \leftrightarrow |4\rangle$, for two orientations of the Cd–S bond relative to the applied field. Part **d** adapted with permission from REF.[132], IOP.

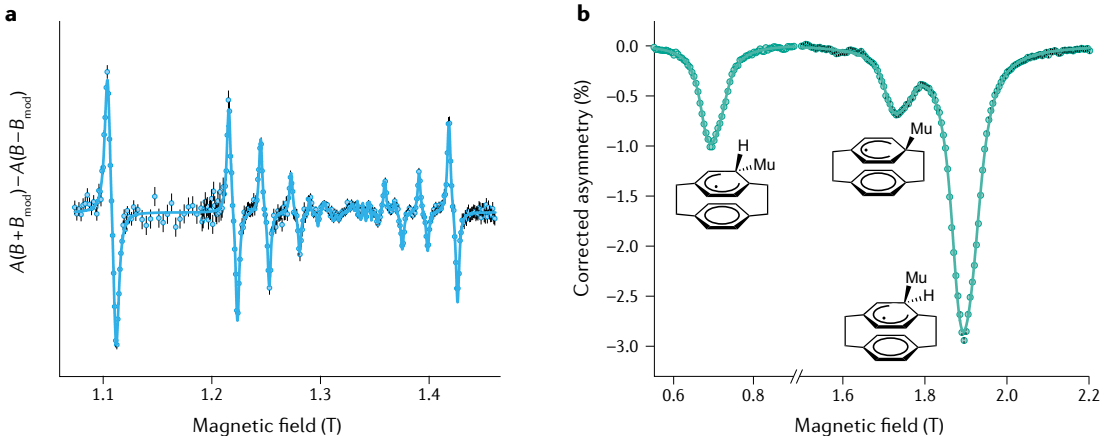

Fig. 4 | **Avoided level crossing muon resonance. a** | Avoided level crossing muon resonance (ALC-μSR) spectrum of the Mu adduct of ^{13}C-labelled C_{60} in decalin solution at 293 K. There are multiple Δ_0 resonances due to the hyperfine coupling with ^{13}C nuclei around the sphere and hyperfine coupling constants were used to map out the distribution of the unpaired electron. Spectrum obtained with magnetic field modulation, which results in resonances having a differential lineshape. **b** | ALC-μSR spectrum of [2.2]paracyclophane at 300 K. Δ_1 resonances of three types of muoniated radicals (chemical image insets) shown. Positions of the resonances give the muon nuclear hyperfine coupling constant, A_μ, of each radical, the widths and line shapes provide information about dipolar muon hyperfine coupling and the amplitudes give relative yield of each radical. Part **a** adapted with permission from REF.[39], Elsevier. Part **b** adapted with permission from REF.[41], ACS.

anything with non-zero spin, such as H, D, ^{13}C, ^{14}N, ^{19}F, ^{31}P and so on. FIGURE 4a shows the ALC-μSR spectrum of the Mu adduct of ^{13}C-labelled C_{60} in decalin solution[39]. There are numerous resonances due to hyperfine coupling between the unpaired electron and the ^{13}C nuclei. The position of the resonances is used with Eq. 10 to calculate the ^{13}C hyperfine coupling constants. This provides information about how the unpaired electron is distributed around the C_{60} sphere.

A Δ_1 resonance is only observed when a muoniated radical undergoes anisotropic motion on a critical timescale. This is given by the inverse of the hyperfine anisotropy, typically ~50 ns for organic radicals. The Δ_1 resonance field only depends on A_μ and is given by:

$$B_{\mathrm{res}}^{\Delta_1} = \frac{1}{2}\left[\frac{A_\mu}{\gamma_\mu} - \frac{A_\mu}{\gamma_e}\right]. \qquad (11)$$

The lineshape of the Δ_1 resonance can be sensitive to the reorientational motion of the muoniated radical[40]. The position of the Δ_1 resonance is used to determine A_μ using Eq. 11 and the line shape can provide information about the anisotropic dynamics. In FIG. 4b there are three Δ_1 resonances due to three types of muoniated radical, which are formed by Mu addition to [2.2] paracyclophane[41].

Elemental analysis

Elemental analysis with negative muons is relatively simple. The intensity of the muonic X-ray peak is directly related to the elemental composition of the sample. However, other contributions can affect the intensity of the peaks, in particular, the probability of muon capture, the cascade transition rates and detector efficiency[42]. The probability of muon capture is, as a first estimate, proportional to the number of electrons — the Fermi–Teller approximation — and in the majority of cases this is sufficient. However, in oxygen-based systems this approximation can be inconsistent. For these systems, additional correction terms are added to take into account the number of loosely bound electrons and the number of valence electrons. Another important factor is the muon cascade probability. A schematic of the cascade for copper is shown in FIG. 2b. This affects the intensities of the muonic X-rays. In general, best practice is to spend time in each experiment measuring certified standards that are close to the expected composition. This enables comparisons of electronic transitions of the different energy levels within the atom, such as K_α, L_α, M_α and other muonic X-rays (FIG. 2c). This also takes into account the detector efficiencies and self-absorption if measured carefully.

During the final nuclear capture process, muons can undergo a reaction with protons to release a neutron(s) and a photon. Neutron release can lead to an unstable nucleus, which subsequently leads to release of γ-rays. The γ-ray energy is of the same magnitude as the muonic X-rays, although the lifetime is generally longer, allowing for relatively easy determination. This means there is a potential for conducting isotope analysis[43] with muons.

Software for analysis

There is a wide range of software available for the analysis of muon spin spectroscopy data; each package is in various stages of development, functionality, sustainability and maintainability. Each muon facility has at least one preferred analysis package. The major analysis packages are MuSRFit[44], WiMDA[45] and Mantid. These packages automatically include numerous corrections that need to be applied to the muon spectra, for example, background, time zero (time of muon implantation) and dead-time corrections. Training can be found by online learning, for example, REF.[46], and assistance from local instrument scientists.

Cascade transition rates
The times taken for a negative muon to cascade between specific energy levels.

Muon cascade probability
The probability of a particular transition between specific energy levels occurring.

Applications

In this section, areas where muon spin spectroscopy is particularly successful are highlighted. The examples covered are magnetism, quantum systems, superconductivity, energy materials, physical chemistry, dynamics in soft matter, semiconductors, surface science, cultural heritage and the effect of muons on electronics. Within each of these sections, key scientific results are discussed and examples presented. As the muon is a local probe, it often provides unique information not obtainable by any other technique. Furthermore, the muons' sensitivity to very weak internal magnetic fields increases its complementarity to other techniques, for example, neutron scattering, NMR, ESR and EPR.

Magnetism

One of the most important applications of muons is in the study of magnetism. In contrast to many other techniques, it is not necessary to apply a magnetic field to obtain a signal; μSR can be performed in zero magnetic field. As a result, any precession signal in the polarization of the implanted muon arises from the internal magnetic field measured at the muon site. This means the temperature dependence of the precession frequency provides the temperature dependence of the order parameter. This makes the muon an efficient indicator of magnetic order, extracting both the strength and magnetic volume fraction in the sample from the frequency and amplitude of the precession signal. Consequently, many magnetic phase diagrams for new material families are often first established by μSR, such as the iron-based superconductors[47–49]. Because the muon probes the entirety of the sample, it is not affected by tiny impurity phases, unlike magnetic susceptibility. This feature permitted the discovery of superexchange via the hydride ion using μSR in a system where nanoscopic elemental cobalt was present as a very minor impurity[50].

The muon is also an effective probe of the dynamics of magnetic moments within a sample. Before materials enter a magnetic ground state, a critical slowing down of the magnetic fluctuations is often observed. Generally, this is seen as a divergence of the muon spin relaxation rate on cooling through the transition. As a result, it can be an effective way of probing the dynamic nature of transitions[51–56], or for providing information on systems where the magnetism is dominated by excitations[57]. Additionally, this approach can also be used to pick apart short and long-range order, where the coupling of the muon to its local environment provides complementary and, sometimes, unique information to other techniques[58–61].

Establishing bulk magnetic order allowed μSR to demonstrate this phenomenon in the very first organic ferromagnet[62,63] based upon free radicals. Muonium attacks the radical and the diamagnetic signal is thought to originate between a singlet state comprising the muonium electron and the radical electron[63]. However, some of the most interesting applications are in low-dimensional magnetic systems. No long-range order is possible in one dimension, but magnetic chains with intrachain exchange, J, occur embedded in crystals and the weak interchain interactions allow long-range order to occur, albeit at much lower temperature than J/k_B (where k_B is the Boltzmann constant) and with reduced moments[64]. In such systems, the thermodynamic signatures of long-range order are strongly suppressed[65], but μSR can easily identify them from the onset of a precession signal (FIG. 5a,b). Therefore, new transitions in molecule-based magnets can be discovered[66], as well as the identification and characterization of one and two-dimensional Heisenberg antiferromagnets[67,68]. These results have been extended to molecular spin ladders[69] and organic molecules showing magnetism and superconductivity[70].

Recent progress in characterizing well-known magnetic compounds, such as MnSi, has allowed exquisite agreement to be obtained between experiment and theory[71]. In addition, μSR has also been applied to study various quantum phase transitions[53,72,73], systems with coupling between magnetism and the lattice[74] and frustrated magnetic ground states[75,76]. Most studies have been in the bulk, but low-energy muons offer the possibility of studying magnetism in thin films and surfaces. A future possibility is to use this to perform proximal magnetometry of spin fluctuations by implanting muons close to a magnetic surface[77].

Interesting effects can occur when the magnetism is not electronic but nuclear. A muon implanted in a fluoride results in a state where the muon resides between two fluorine ions: F–μ–F[78]. An oscillatory time dependence of muon polarization can result from entanglement of the muon and its nearest-neighbour spin-1/2 fluorine, which arises due to magnetic dipolar interactions[78,79]. Distant nuclear spins in the system can result in a decohering effect that may be modelled quantitatively. This allows for a detailed description of the decoherence coupling processes in the F–μ–F system with its environment, providing a model realization of the quantum decoherence problem[80].

Quantum systems

In quantum magnets, the rotational symmetry of the spins is preserved in the ground state. This is different to classical magnets with long-range, ordered spins and spin glasses, which all feature on-site static moments at low temperature. In addition, these features are also unlike paramagnets because strong correlations exist between the spins, leading to non-trivial ground states and exotic excitations. Implanted muons allow scientists to select magnetic materials with a ground state dominated by quantum fluctuations, and to probe the nature of their original excitations, both of which can be performed with unique accuracy.

To favour such quantum states, the quantum fluctuations have to be strongly enhanced. This is best achieved in low-spin $S = 1/2$ materials, such as the widely studied cuprates, and $S = 1/2$ molecular magnets or, less commonly, vanadium[81] or titanium-based oxides[82]. Alternatively, effective quantum spins may be realized in heavier transition metal oxides with large spin–orbit coupling, such as iridates, or in the low-energy physics of some rare earth-based magnets.

The dimensionality of the spin system is another important parameter for quantum magnetism. In spin

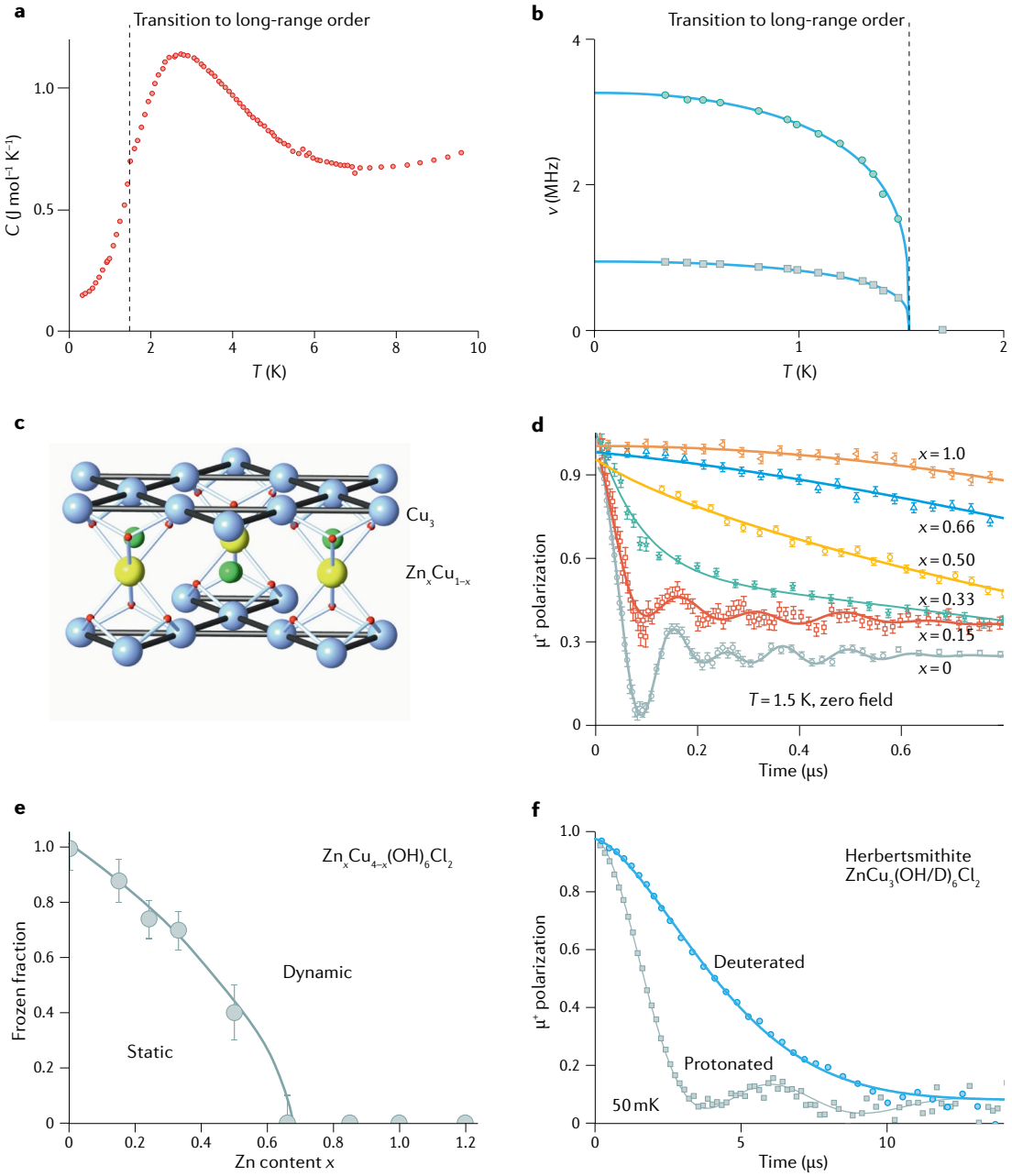

Fig. 5 | **Applications in copper-based systems. a,b** | Heat capacity (part **a**) and muon spin rotation/relaxation/resonance (μSR) precession frequencies (part **b**) measured in $[Cu(HF_2)(pyz)_2]BF_4$ (where pyz = pyrazine). Broad peak in heat capacity due to building correlations in two-dimensional planes. Three-dimensional long-range order only sets in once the inter-plane interactions become important, but the transition to long-range order (indicated by vertical dashed line) is not clearly visible from heat capacity data. By contrast, clear precession signal consisting of two frequencies is found in muon experiments and these data allow the order parameter to be tracked. **c** | Crystal structure of paratacamite compounds. Spin liquid candidate herbertsmithite is obtained for $x = 1$, when the copper-based kagome planes are separated by diamagnetic zinc. **d** | Muon depolarization spectra show that static internal fields vanish progressively as x increases. **e** | Magnetic phase diagram of paratacamite drawn from the μSR data shown in part **d**. **f** | In herbertsmithite ($x = 1$), relaxation is mostly due to quasi-static nuclear magnetism. μ^+, positive muon. Parts **a** and **b** adapted with permission from REF.[202], RSC. Parts **d**,**e** and **f** adapted with permission from REF.[83], APS Physics.

chain or spin ladder compounds, the low dimensionality efficiently suppresses the development of long-range order in favour of quantum ground states. This is the case in the quasi-one-dimensional regime of the material, when the temperature is larger than the interchain or inter-ladder residual interaction[66]. μSR is uniquely suited to single out the relevant — most often low — energy scales which require sub Kelvin and non-perturbative zero field experiments.

In higher dimensions, avoiding long-range order is more challenging. It requires a high level of frustration of the magnetic interaction, which can arise from

Cooper pairs
Pairs of electrons that are bound together by a weak force, and required for superconductivity.

competing interactions; the geometry of the lattice, as observed in well-studied kagome materials that feature a corner-sharing triangular magnetic lattice[83]; or strongly anisotropic, bond-dependent, interactions as in Kitaev materials[84]. The various quantum ground states expected in such conditions are generically dubbed quantum spin liquids. One common signature of these quantum spin liquids is the absence of static magnetism, even at $T = 0$ K. The unique sensitivity of μSR to tiny static internal fields makes it an ideal probe to test this simple requirement[83] and is now commonly applied to newly discovered spin liquid candidate materials at the early stage of their investigation[85]. In particular, μSR has proved invaluable to reveal subtle magnetic ordering with weak frozen moments, a disordered spin glass-like state and/or inhomogeneous ground states that are often realized in low-dimensional frustrated materials that fail to retain a spin liquid state[86] or are driven beyond a quantum critical point by external pressure[84] or applied fields[75]. FIGURE 5c–f shows how static long-range order is progressively suppressed upon zinc doping of the antiferromagnet $Cu_4(OH)_6Cl_2$ to form herbertsmithite, $ZnCu_3(OH)_6Cl_2$. For intermediate doping, both a paramagnetic phase and a frozen, strongly disordered, magnetic phase coexist. In the herbertsmithite spin liquid end member, only the static nuclear magnetism depolarizes the implanted muons. The electronic spins are fast fluctuating or entangled in a non-magnetic singlet ground state.

Beyond asserting the absence of frozen magnetism, detailed study of the dynamical relaxation and how it evolves with temperature or applied longitudinal field can provide information about the nature of the excitations[87,88]. These excitations are often exotic in quantum disordered materials[69] — either confined or unconfined, from neutral fermion forming a metal-like Fermi sea to Dirac or Majorana fermions, with a gap or gapless spectrum — and are often characteristic of the otherwise elusive nature of the spin liquid state.

Superconductivity

The discovery of superconducting cuprate and iron pnictide compounds with high transition temperature (T_c) has fuelled a flurry of research into superconductivity. There has been a huge theoretical and experimental effort to understand the mechanism of unconventional superconductivity and to search for higher-temperature superconductors, due to the potential widespread applications of superconductor materials. Muon spin rotation/relaxation has proved an effective probe of superconductivity in many different classes of materials.

Transverse-field μSR has been widely used to probe the internal magnetic field distribution in the vortex state of type II superconductors[89,90]. In a transverse-field μSR experiment, spin-polarized positive muons are implanted into a sample in an external field perpendicular to the initial muon spin polarization. Each muon precesses around the local field at its site, and the functional form of the muon spin polarization depends on the field distribution of the flux-line lattice of the vortex state, which is determined by the magnetic penetration depth, λ, the vortex core radius, r, and the structure of the flux-line lattice. The muon spin relaxation rate is related to the root mean square width of the internal magnetic field distribution in the flux-line lattice. In turn, the root mean square width is inversely proportional to the square of the magnetic penetration depth λ, which is related to the density n_s of superconducting carries and m^* by the London equation[91]:

$$1/\lambda^2 = \mu_0 n_s e^2/m^* \quad (12)$$

Therefore, the temperature dependence of normalized superfluid density can be measured by transverse-field μSR, and the functional form of $n_s(T)$ depends on the gap symmetry. Evidence of d-wave superconductivity for cuprate[92] and multiple gap symmetries for the order parameter without nodes for iron pnictides[93] have been given. The famous Uemura plot, in which T_c is plotted as a function of effective Fermi temperature evaluated from $1/\lambda^2(0)$, as determined by μSR, established universal behaviour for different categories of superconductors, covering dynamic superconductivity observed recently[94,95]. The precession frequency of a paramagnet is shifted from its value in vacuum during a high transverse-field μSR experiment. The fractional frequency shift, the Knight shift, provides a microscopic characterization of the static magnetization. In a superconducting state, Knight shift includes the contribution from spin susceptibility and study of it provides crucial information about the pairing symmetry of Cooper pairs[89].

One of the important properties of superconductivity is whether or not time-reversal symmetry (TRS) is broken[96]. Superconducting states with broken TRS have Cooper pairs with non-zero magnetic moments. Local alignment of these moments results in extremely small internal magnetic fields. Zero-field μSR is one of the most powerful methods for detecting such small, spontaneous magnetic fields because it is sensitive to small changes in internal fields and can often measure fields of 10 μT, equivalent to a precession frequency of 1.5 kHz (REFS[89,97]). When magnetic order is not present, the muon spin polarization is only relaxed by static, randomly orientated nuclear dipole moments. This relaxation rate is temperature independent. Consequently, if a weak, spontaneous internal field appears below the superconducting transition temperature, T_c, there is an increase in the relaxation of muon spin polarization. In this situation, the increase in relaxation corresponds to an order parameter. TRS-broken superconducting states are rare; however, μSR has successfully detected this phenomenon in numerous unconventional superconductors, such as the layered perovskite superconductor Sr_2RuO_4 (REF.[98]), non-centrosymmetric $LaNiC_2$ (REF.[99]) and the filled skutterudite compounds $PrOs_4Sb_{12}$ and $PrPt_4Ge_{12}$ (REFS[100,101]). A recent topical review of the muon details the results of TRS breaking superconductors[102].

There is growing evidence for the coexistence of superconductivity with either ferromagnetic or antiferromagnetic ordering. However, there is currently no unified theory for the coexistence of superconductivity and magnetism. This interplay of magnetism and superconductivity has been a central problem in condensed

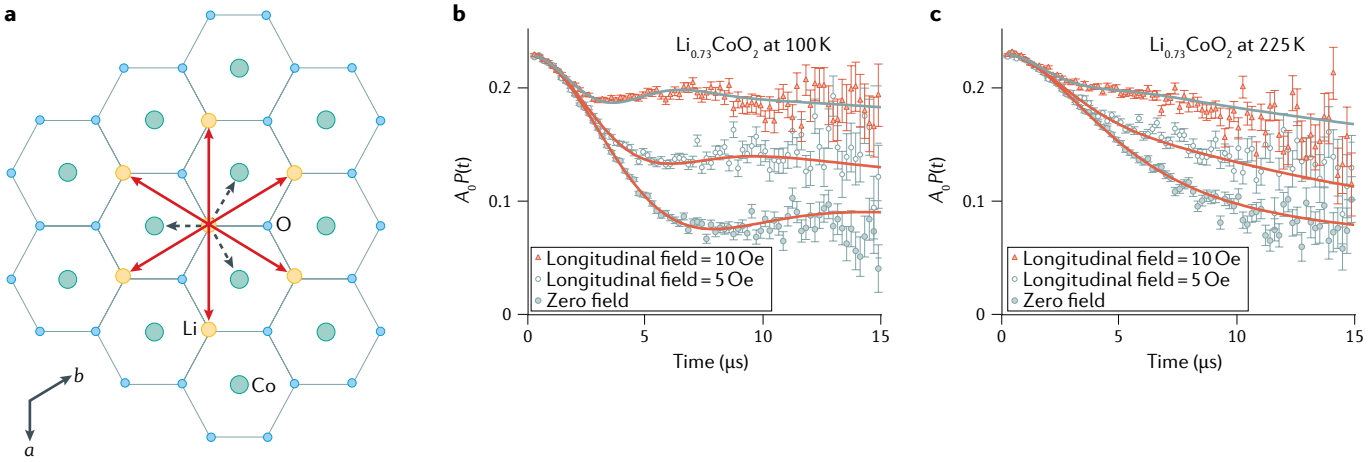

Fig. 6 | **Li⁺ diffusion in battery materials. a** | Schematic of path for lithium diffusion in Li_xCoO_2. **b**,**c** | Zero-field muon spin (zero-field μ⁺SR) spectrum exhibiting a Kubo–Toyabe-type relaxation for $Li_{0.73}CoO_2$ at 100 K (static) (part **b**) and at 225 K (dynamic) (part **c**). *a* and *b*, crystal axes; μ⁺SR, positive muon spin rotation/relaxation/resonance. Parts **a**, **b** and **c** adapted with permission from REF.[107], APS Physics.

matter physics. Because of μSR's high sensitivity to internal magnetic fields on a microscopic scale, in addition to its ability to determine the volume fraction of the magnetic and superconducting phases, plus the temperature or doping dependence of order parameters, the method has been successfully applied to study the interplay of magnetism and superconductivity in various unconventional superconductors. For example, a μSR investigation of an iron pnictide $SmFeAsO_{1-x}F_x$ with $x = 0–0.30$ shows that static magnetism persists into the superconducting regime[48]. On the other hand, a μSR study showed that the magnetic order region competes with the superconductivity in the $La_{2-x}Sr_xCu_{1-y}Zn_yO_4$ system[99,103]. In addition to static magnetism, the μSR technique is also capable of detecting dynamic magnetism and has revealed slowly fluctuating magnetic fields in the pseudo-gap region of the high-temperature superconducting cuprates[104].

Energy materials

In this section, the ways in which μSR can be applied to research energy materials, such as electrode materials for lithium-ion batteries and hydrogen storage materials, are demonstrated. In battery electrode materials, Li⁺ ions diffuse between regular lithium sites and vacant sites (FIG. 6a). This diffusion is a key factor for determining the charge and discharge rates of a battery.

The timescale of Li⁺ diffusion in battery materials is within the time window for the μSR technique[105,106]. Although Li-NMR is a suitable probe to detect ion diffusion, signals from magnetic ions such as cobalt and iron, which are contained in battery materials, hinder the observation of Li⁺ diffusion. In the μSR technique, responses from Li⁺ diffusion and magnetic ions appear with completely different frequencies that can be distinguished. Therefore, μSR can act as a unique probe of Li⁺ diffusion in battery materials. The zero-field μSR with positive muons (μ⁺SR) spectrum for $LiMO_2$ usually exhibits a well-known Kubo–Toyabe-type relaxation behaviour (FIG. 6b), and such a spectrum can be easily decoupled with a small longitudinal field, typically below 1 mT, comparable with the field distribution width at the muon sites[107]. When lithium starts to diffuse, the relaxation rate is suppressed owing to motional narrowing (FIG. 6c). A similar diffusive behaviour is also exhibited by sodium-ion battery materials[108,109]. A recent study using μSR with negative muons (μ⁻SR) on $LiMnPO_4$ demonstrated that this behaviour is not caused by μ⁺ diffusion but by Li⁺ diffusion[110]. This is because μ⁻ are captured by the nucleus and information about nuclear magnetic fields is typically provided from fixed viewpoints. Such examples illustrate the complementary use of both positive and negative muons in studies on ion diffusion.

The technique of μSR is a good tool for detecting hydrogen diffusion in hydrogen storage materials during desorption reaction with controlling temperature. This variable is important because a lower hydrogen desorption temperature, T_d, is required for hydrogen storage materials. A pioneering μ⁺SR study has been reported on $NaAlH_4$, where a three spin-1/2 system H–μ–H is formed[111]. Additionally, formation of H–μ–H and H–μ were found in numerous hydrogen storage materials including MgH_2 (Supplementary Fig. 1a,b)[112] through observation of a characteristic oscillation in the zero-field μ⁺SR spectrum (Supplementary Fig. 1c). Recent in situ μ⁺SR work on MgH_2 (REF.[112]) demonstrated that the H–μ–H system disappears above room temperature and that the zero-field μ⁺SR spectrum instead exhibits a Kubo–Toyabe-type relaxation behaviour (Supplementary Fig. 1d). Additionally, with further increases in temperature, hydrogen starts to diffuse below T_d (Supplementary Fig. 1e)[112]. To decrease T_d, it is important to enhance hydrogen diffusion in MgH_2 in order to release the desorbed H_2 from the system[112]. Research on μSR with MgH_2 has also supported the presence of hydrogen diffusion in MgH_2 (REF.[113]).

Physical chemistry

The main use of μSR in physical chemistry is to study the reactions of muonium ($Mu = [\mu^+e^-]$) and to characterize free radicals[37]. Muonium is studied because it is similar to, yet different from, hydrogen. The similar chemical behaviour of Mu and hydrogen means that Mu is studied

in conditions where it is not possible to study hydrogen, such as inside a pressure cell. High-momentum muons are highly penetrating and the decay positrons, which provide the information about the evolution of the muon's spin polarization, are energetic enough to escape the pressure vessel. Mu can also be generated cleanly whereas hydrogen atom formation by radiolysis produces multiple reactive species, such as •OH, e_{aq}^-, HO_2• and H_2O_2 in water, which requires the addition of scavengers and complicates analysis.

A key difference between Mu and hydrogen is the light mass of Mu — one-ninth that of hydrogen — which can lead to large isotope effects that provide information about the mechanism of the reaction being studied. For example, the addition of Mu to benzene in the gas phase[114] is more than an order of magnitude faster than that of hydrogen or deuterium addition[115] at room temperature (FIG. 7a), due to tunnelling playing a dominant role. This should be compared with the Mu + $CH_3OH_{(aq)}$ abstraction reaction[116], which is approximately two orders of magnitude slower than the H + $CH_3OH_{(aq)}$ reaction[117,118] (FIG. 7b). Abstraction reactions typically have barriers that are too wide for tunnelling, and the inverse kinetic isotope effect — the reaction being slower for the lighter isotope — is primarily due to the activation energy of the lighter isotope being larger because of higher zero-point vibrational energy in the transition state[119]. The Mu + $CH_3OH_{(aq)}$ reaction was studied to much higher temperatures than was possible for H + $CH_3OH_{(aq)}$ and this enabled observation of deviations from Arrhenius behaviour close to the critical point of water. The temperature dependence of the H + $CH_3OH_{(aq)}$ reaction rate can be predicted from the results of the μSR measurements.

μSR can be used to characterize the structure and dynamics of radicals in a way that is similar to EPR[37]. Transient radicals have an important role in chemistry, such as intermediates in reactions, but are difficult to study with most conventional spectroscopic techniques due to their short lifetimes. Radicals can be identified by measuring the muon and nuclear hyperfine coupling constants, which map out the distribution of the unpaired electron, and then comparing these values with ones obtained from ab initio calculations. Information about dynamics as well as the conformation can be obtained by measuring the temperature dependence of the hyperfine coupling constants.

There are several advantages of using μSR over EPR for studying transient free radicals. First, muoniated radicals are produced in situ and do not require the addition of harsh chemicals, for example, Fenton's reagent, or radiolysis with electrons or γ-rays. Alongside this, muons arrive with almost 100% spin polarization. This means very low quantities of muoniated species can be detected: 10^7 compared with 10^{12} spins for ESR and 10^{18} for NMR. Additionally, μSR does not require an external electromagnetic field to stimulate spin-level transitions and very short-lived radicals can be detected. Furthermore, higher-temperature EPR measurements of transient free radicals can be difficult as bimolecular termination reactions lead to a loss of signal. By contrast, at any given instant there are only a few muoniated radicals in a sample, meaning bimolecular termination reactions can be ignored. This makes it possible to study radicals under conditions where they are highly mobile, such as at high temperatures. Finally, muoniated radicals are usually the primary product of the Mu addition reaction. This is advantageous as EPR spectra are frequently complicated by secondary and later products.

However, μSR has difficulty dealing with systems with multiple unsaturated bonds. The relative yield of different muoniated radicals depends on the number and reactivity of the different functional groups in the parent compound(s). Although this does provide a means of probing the reactivity of a parent compound, the more radicals that are formed, the more difficult it is to characterize them because the polarization will be distributed among them, resulting in lower signal amplitudes.

Consider the reaction of Mu with a phosphaalkene (FIG. 7c **1**), which is a molecule with a P=C bond[120]. Mu could add to either the phosphorous atom or the carbon atom and generate the radicals shown in FIG. 7c. Two types of muoniated radical were observed in the transverse-field μSR spectrum (FIG. 7d) and they have different yields. There were two resonances at lower magnetic fields (Supplementary Fig. 2a) due to hyperfine coupling with phosphorous, and one resonance at a higher magnetic field (Supplementary Fig. 2b) due to hyperfine coupling with the protons of the two methyl groups. The magnitude of the muon, phosphorous and proton hyperfine coupling constants were used to assign the structures, and this was aided by a comparison with a structurally related radical. In FIGURE 7c, **1b** was determined to be the major product and **1a** was the minor product.

Dynamics in soft matter

Studying the dynamics of molecular units is vital to understanding the properties of soft matter, such as liquid crystals and biomembranes. Mu will add to unsaturated bonds in soft matter to produce muoniated spin labels in specific sites that are sensitive to the local environment and dynamics. The muoniated radicals, which are present in extremely low concentrations, are small perturbations to the system whereas fluorescent probes and nitroxide spin labels have been found to significantly alter the properties of membranes[121]. The site-directed muon spin labelling, plus the sensitivity of μSR to motion on different timescales compared with NMR and X-ray and neutron scattering, means μSR can provide unique and complementary information from other techniques.

The following examples consider molecules that interact with bilayers, such as fragrances interacting with soap, or drug molecules interacting with biomembranes. For instance, DHTAC (2,3-diheptadecyl ester ethoxypropyl-1, 1,1-trimethylammonium chloride) (FIG. 7e) is a molecule that has hydrophobic and hydrophilic functional groups. It can self-assemble in aqueous solution to form different structures, such as lamellar liquid crystalline phases, where the surfactant molecules form arrays of regularly separated bilayer sheets separated by solvent[122].

Abstraction reaction
This reaction involves the abstraction of an atom from a molecule. The abstracting species is usually a radical species itself. Mu may abstract a hydrogen atom from a C–H bond in saturated organic molecules, leading to the formation of a diamagnetic MuH molecule and a non-muoniated radical.

Zero-point vibrational energy
The lowest energy of a quantum mechanical system, which is non-zero because of quantum mechanical fluctuations.

The addition of co-surfactants results in subtle changes in the microstructure of the bilayer, which, in turn, has dramatic effects on macroscopic behaviour (see REF.[123]). Co-surfactants have additional roles, such as being a fragrance or a pharmaceutical, and are typically present only in very low concentrations (approximately millimolar), making them difficult to study using traditional spectroscopic methods[124].

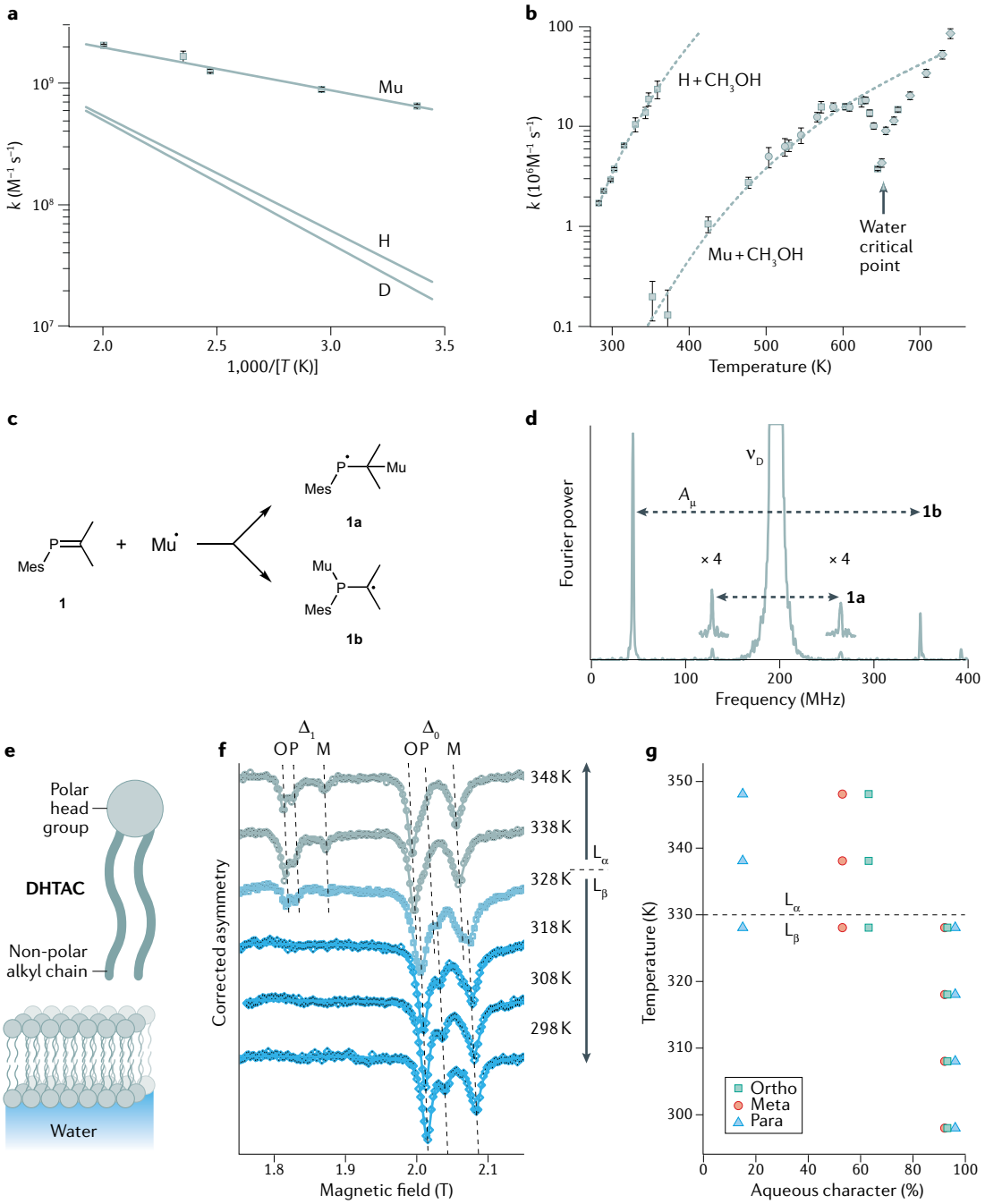

Fig. 7 | **Muoniated radicals. a** | Arrhenius plots for addition reactions of Mu, hydrogen and deuterium to benzene in the gas phase. **b** | Rate constants for reaction of Mu with methanol in water at ~230 bar and hydrogen with methanol at ambient pressure. **c** | Structures of phosphaalkene (**1**) and the possible muoniated radicals (**1a** and **1b**). **d** | Transverse-field muon spin rotation (μSR) spectrum of a solution of phosphaalkene **1** in THF. The radical signals are equally spaced about the diamagnetic muon precession signal, ν_D, and the splitting is equal to A_μ, the muon hyperfine coupling constant of the muoniated radical. **e** | Structure of DHTAC (2,3-diheptadecyl ester ethoxypropyl-1,1,1-trimethylammonium chloride) and schematic of bilayer with locations of 2-phenylethanol (PEA) in the low-temperature L_β phase and high-temperature L_α phase. **f** | Avoided level crossing muon resonance (ALC-μSR) spectra of PEA in DHTAC bilayers. O, M and P refer to muoniated radicals formed by Mu addition to ortho, meta and para carbons of phenyl ring of PEA. **g** | Local polarities determined from Δ_0 resonance fields. D, deuterium atom; *k*, rate constant for the reaction; ν_D, magnetic muon precession signal. Part **a** data from REFS[114,115]. Part **b** data from REFS[116–118]. Parts **c** and **d** adapted with permission from REF.[120], Wiley. Parts **f** and **g** adapted with permission from REF.[125], ACS.

ALC-μSR can be used to determine where the co-surfactant is located. The co-surfactant 2-phenylethanol (PEA) gives an odour of roses in DHTAC bilayers[125] (FIG. 7e–g). Muoniated radicals are formed by Mu addition to the ortho, meta and para carbons of the phenyl ring of PEA. However, Mu addition to DHTAC does not form muoniated radicals because the Mu addition to C=O bonds is ~100 times slower than to phenyl rings. The hyperfine coupling constants of Mu adducts of PEA — and, hence, the Δ_0 resonance positions — are sensitive to the polarity of the local environment of PEA. Shifts of the Δ_0 resonances in a range of solvents were used to determine the aqueous character of the environment ranging from water (100% aqueous) to $C_{18}H_{38}$ (0% aqueous).

At 329 K, DHTAC bilayers undergo a structural change. Below this temperature, the L_β phase is formed and motion of the alkyl chains is limited. Above 329 K, the system is in the L_α phase and the alkyl chains have considerably more mobility. In the L_β phase, there are three Δ_0 methylene proton resonances but no Δ_1 resonances. This indicates isotropic motion of the radical and the co-surfactant. The aqueous character of the three isomers is close to 100% (FIG. 7f). Combined, these observations indicate that PEA cannot penetrate the bilayer in the L_β phase due to tight packing of the alkyl chains. Instead, PEA resides in an aqueous environment. By contrast, in the L_α phase, Δ_1 resonances are observed. This suggests that the radicals have anisotropic motion and the Δ_0 resonances have shifted to a lower magnetic field, consistent with less aqueous character. Overall, the results indicate that, in the L_α phase, PEA resides within the DHTAC bilayer due to the greater mobility of alkyl chains in the bilayer. At 328 K, near the L_β–L_α transition, PEA resides in both the bilayer and the aqueous region.

Semiconductors or hydrogen in materials

Hydrogen is an unavoidable contaminant in most semiconductors as it is easily incorporated in all steps of the material handling, from growth to processing. In addition to the formation of complexes, hydrogen can be present in semiconductors as an isolated, monoatomic impurity, most commonly playing a compensating role. Although isolated hydrogen has an important electrical activity, when present in very low concentrations it is often not accessible by conventional techniques, making the μSR technique a unique tool for its study. When the positive muon is incorporated in the semiconductor, it may bind to an electron and form muonium, which behaves as a light isotope of hydrogen with very similar electronic properties. Muon implantation inside a semiconductor material creates muonium impurities in the high-dilution limit, with three possible charge states, Mu^+, Mu^0 and Mu^-, mimicking the charged states of isolated hydrogen (H^+, H^0 and H^-). The correspondence between the hydrogen and muon impurity centres is well supported by the few cases where the experimental observation of both systems was conducted, namely in silicon, ZnO and TiO_2 (REFS[126–131]). Most of the existing information on the role of isolated hydrogen in both elemental and compound semiconductors was obtained by the μSR technique, namely concerning Mu configuration, position of electronic levels, interaction with carriers as well as passivation of impurities and defects[132]. Prior to μSR results, hydrogen was known to occupy interstitial positions in the host material, either as a neutral or a negatively charged centre (H^-/H^0) that introduces an acceptor level in the band gap. Among the numerous contributions of μSR to the physics of hydrogen in semiconductors, of importance is the discovery and characterization of two other possible isolated hydrogen configurations, incorporated into the bonding structure of the lattice. One is a bond-centre configuration, first observed and extensively characterized in silicon by μSR, together with the corresponding deep donor level[126,132]. The second is the finding of a shallow donor state in some materials, where the muon (or the proton) stabilizes in an anti-bonding position, close to an anion[127,133] (FIG. 3). μSR results in ZnO constituted the first experimental confirmation of a theoretical suggestion that hydrogen would be a cause of n-type doping in this important material[127].

Recently, muons were explored as a local probe to charge carriers and defects in semiconductors. One route is direct interaction with charge carriers in photo-excited samples. Examples include measuring of excess carrier lifetimes[134] and the observation of the hole carrier density profile at a film surface[29]. A different route relies on the sensitivity of the relative fractions of the different muon charge states to the defect content of the material and the possibility to obtain depth-resolved information on defective layers in films, using slow muons[135,136].

Surface science

The application of low-energy muons (low-energy μSR) to thin films and near-surface studies is a growing field. One of the most straightforward applications is measurement of magnetic field profiles at the surface of superconductors to directly determine the penetration depth and coherence length[137–140]; measurement of the shape of domains in type I superconductors[141]; or measurement of proximity effects between superconducting and non-superconducting thin layers of metals, ferromagnetic layers and topological materials[142–147]. These studies reveal the strength and sensitivity of low-energy μSR for determining magnetic field profiles with nanometre resolution at interfaces, allowing new insights into anomalous proximity effects — such as the newly discovered electromagnetic proximity effect[144–146] — and induced odd-frequency superconductivity[143,147].

The effect of dimensionality and strain on the magnetic and superconducting properties of thin film heterostructures is another wide field of low-energy μSR applications. Two pioneering works showed the drastic effect of dimensionality on the magnetic order. The first work combined optical ellipsometry and low-energy μSR to demonstrate that paramagnetic and metallic $LaNiO_3$ could be controlled to become insulating and antiferromagnetically ordered, if the layer thickness is reduced to two unit cells, independent of the strain of the film[148]. In this quasi-two-dimensional system, the tendency towards charge and spin order is thought to be due to enhanced nesting of the $LaNiO_3$ Fermi surface, similar to bulk $RNiO_3$, where R is a small-radius rare-earth anion. The second work showed that for

High-dilution limit
The limit approached when the muon is in extreme dilution where there are no muon–muon interactions due to the scarcity of the muon.

La_2CuO_4 layers the long-range magnetic order breaks down for fewer than five layers of CuO_2. At this point, a magnetic state evolves with enhanced quantum fluctuations and reduced spin stiffness[149]. Surprisingly, the state exists in close proximity to a superconducting layer without transmitting supercurrents. In other, complex cuprate metal oxide correlated electronic systems, an interplay between quasi-two-dimensional superconductivity and magnetism was observed in superlattices of δ-doped La_2CuO_4 (REF.[150]). Single layers of SrO_2 periodically inserted in a lattice of LaO_2 layers provide charge doping to turn the interface of the LaO_2 layers superconducting. A non-trivial coupling of the superconducting state ($T_c \sim 25$ K) to the antiferromagnetic order ($T_N = 325$ K) occurs. Below T_c there is a strong increase of the magnetic volume fraction. This is attributed to a charge redistribution of free carriers at close proximity between the different layers when the superconducting gap opens. The effect of strain and defects on the magnetic transition temperatures was investigated in a series of experiments on cuprates[151] and manganites[152–154]. Defects typically cause a reduction of magnetic transition temperatures, whereas strain can lead to both increase and decrease, depending on the type of strain.

Films of dilute ferromagnetic semiconductors and their magnetic homogeneity are important for spintronics applications. Using low-energy μSR, it is straightforward to measure the magnetic volume fractions of these systems, enabling determination of the appropriate growth and annealing conditions to generate homogeneous systems[155–158]. If the film thickness is less than 100 nm, the muons can be implanted in the substrate to measure the magnetic stray fields from the ferromagnetic layers. The size of the stray fields and the length scale of its disappearance provide information about the interface roughness and the multi-domain character of the film[158,159].

By localizing the region of magnetic moments inside heterostructures, low-energy μSR derived significant information about spin diffusion in organic spin valves[159], the emergence of ferromagnetic order at metal/C_{60} interfaces[160], spin storage in metal oxide/C_{60} interfaces[161] and depth dependence of spin dynamics in molecular magnetic systems[162,163]. In semiconductor physics, low-energy μSR extends the classical μSR application of characterizing hydrogen impurities to new directions. For example, it was applied to investigate defect regions at interfaces in solar cell materials[135], in 4H–SiC[136] to provide microscopic information to improve interfaces for device applications, and to study band bending[164], charge carrier profiles and their manipulation at semiconductor surfaces[29].

These examples represent some of the highlights of low-energy μSR applications. There are many more possibilities, and a complete list can be found on the Low-Energy Muons Group website.

Cultural heritage

Recent developments at muon facilities have shown a resurgence in using μSR to analyse materials with a cultural heritage interest. It is of particular interest to use this technique because it is sensitive to all elements — although hydrogen and helium are challenging — can probe deep within a sample, can be depth-dependent and, most importantly, is completely non-destructive. A recent example of the potential of this technique for heritage applications was the investigation of debasement of coinage from various historical perspectives[165]. A particular period of interest is the Roman Empire, where silver coinage was actually a silver–copper alloy. Coins were subjected to heat treatment and oxidation to enrich the surface, allowing the silver composition to vary from 100% to as low as 20%[166,167]. It is argued that establishing the composition of these coins yields new and valuable information about the fiscal health of ancient nations. The results from REF.[165] show the extent of the surface enrichment as shown in FIG. 2c,d. However, it would appear that the gold coinage was left untouched, even in times of great turmoil[168].

Alongside Roman coins, other gold coinage was also surface enriched. An example is a coin from the Tempo Koban (nineteenth century CE) in which the core composition is approximately 57 wt% gold and 43 wt% silver[169]. A recent study of votive lamp fragments in the form of small ships showed a range of compositions of Cu–Sn–Pb[170]. Although these examples are metallic samples, there is no reason why other materials, including organic samples, cannot be investigated. An early example of this is the modern and archaeological fired clays[171] and biomaterials[172,173]. This clearly shows the versatility and general application of the technique to all materials, whether that be cultural heritage or not. A more detailed review can be found in REF.[174].

Effects of muons on electronics

Neutron and alpha-radiation are dominant causes of radiation-induced electronics failure. On earth, neutrons are prevalent, whereas protons and heavy ions are of most concern in space. The primary source of cosmic radiation is high-energy protons, with ~87% creating neutrons and muons, and the remainder consists of α-particles (~11%) and high-energy electrons (~1%). On the earth's surface, muons that result from the interaction of high-energy protons contribute to about 75% of the dose rate. These muons are, generally, of very high energies and in the range of 1–20 GeV. However, as electronic technologies reduce in size and power, the risk of negative effects from singly charged particles, in particular muons, increases. In older technologies, charged particles such as muons travelling through the device did not disturb the atomic environment significantly enough for a soft error to occur[175]. However, as the technologies reduced in size, more soft errors are observed. To understand the effects of muons on electronics, and where the electronics are most sensitive, the muon implantation depth can be controlled. It has been found that the error rate increased when the muons were implanted directly into the active electronic layer[176,177]. These 'soft errors' were further enhanced when the bias voltage decreased, something that is desirable for end users as it enables the battery to last longer. Furthermore, it has recently been found that the error rate was enhanced with negative muons[178]. Experiments at muon facilities provide

Soft error
An error in electronics where a bit has been changed by an external source, generally through some interaction with particles and/or radiation.

valuable insights into these errors in a short and controlled timescale, which supports the development of new and reliable electronics.

Reproducibility and data deposition

Raw data are usually stored at the facility, with a range of access policies. At the start of each experimental cycle the instruments are calibrated. This includes ensuring the focus of the beam is optimized for each instrument, and checking that the detectors, the data acquisition systems and the electronics are functioning properly. In addition, this also involves a determination of the time the muon enters the sample, known as t_0, and at pulsed sources evaluating the dead time of each detector. This calibration data should be readily available and may be stored in the data files.

When reporting results from a muon experiment, the facility (this could be via a data DOI), the instrument or instrument(s) used and the set-up of the instrument/beamline should be cited. To ensure reproducibility, the sample environment used and how the sample was mounted should be included. When reporting the sample environment, it is beneficial to be specific about which piece of equipment is used. This enables the exact set-up to be reproduced in the future. Each facility has a standard format with readers that are freely available but, unfortunately, each has its own preferred format. The data are made freely available to all through the facility website, although this might be delayed until after an embargo period, for example, 3 years to ensure a PhD thesis can be completed. The data files are, currently, relatively small, at most only a few megabytes.

Limitations and optimizations

This section discusses aspects that should be considered to ensure a successful experiment, including a section on how to obtain beamtime at a muon facility.

Time window

A key consideration for any experiment is whether the muons are measuring in a frequency range of interest. Muons have a very broad time window when measuring relaxation time (FIG. 8a), ranging from 10^{-4} to 10^{-11} s. However, each type of muon facility has an optimized region to work in. Generally, for fast relaxations and/or high precession frequencies, a continuous muon source is optimal. However, for slower relaxations and when many muon lifetimes need to be measured and/or low-frequency pulsed stimuli, then a pulsed muon source may be optimal. Of course, there is a wide overlapping range of each facility and even beamlines.

Sample size and mass

The mass and size of a sample are important to consider during sample mounting. For example, a small sample with a big sample holder can be problematic and it may be beneficial to create a silver foil packet to contain the sample. This is where a competition between beam spot size, experimental statistics and the areal density of the sample comes into play. In many facilities, it is possible to vary the beam spot size, but this is normally at the cost of count rate. To optimize this, the range of the instrument in a specific sample environment should be considered using a degrader curve. The degrader curves shown in FIG. 8b were made by using a haematite plate, where titanium foils were added to probe the stopping profile of the muon beam in two different sample environments. Even external stimuli sample environments can be developed. From this, the median value required to stop the majority of the muons and the areal density needed to stop all of the muons within the sample may be deduced. This is dependent on the beamline, cryostat and number of beam windows. If the sample is insufficient to stop all of the muons, a degrader in

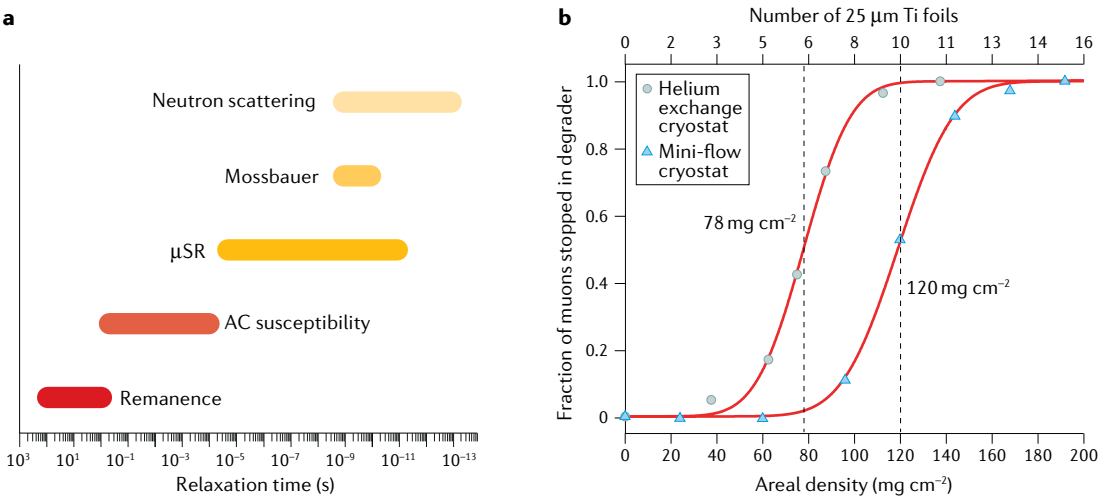

Fig. 8 | **Time windows and degrader curves. a** | Time window of various techniques, highlighting the versatility of muons and the limitations. **b** | Degrader curves for two different sample environments taken on the ARGUS spectrometer within the RIKEN-RAL facility at the ISIS Neutron and Muon Source using 25 μm titanium foil. Dotted lines indicate median value for each degrader curve, which shows the areal density at which the majority of muons are stopped within the degrader, or, in reality, the sample. In an ideal experimental situation, there should be enough areal density to stop all muons within the sample, corresponding to the point where the fraction of muons stopped in the degrader material is equal to one. μSR, muon spin rotation/relaxation/resonance.

the form of titanium, silver or mylar foils can be used. If using a transverse field measurement, the background term can be minimized by mounting a sample on a haematite plate. The muons that stop in the haematite are dephased extremely rapidly and are not seen in the muon spectra.

With particularly small samples, for a facility or beamline this is usually a few millimetres by millimetres, there are two main methods to overcome the small sample size. The first is to use fly past, where the sample is mounted on a holder similar in size to the sample and the excess muons fly past the sample into a long tube further down from the instrument, where their decay has no or limited impact on the measurement. The second is to use a veto method, such as that at PSI and TRIUMF, where muons that stop outside the sample are detected, but can be vetoed and not counted within the spectra.

Access to facilities

The beamtime available for muon experiments globally is fairly limited; there are currently only five operational muon facilities. Each facility has a range of access mechanisms: rapid access for urgent studies — including, but not limited to, very topical material, short life of the sample, data needed for a thesis and/or publication — industrial access and, the most common, general access call. The general access calls are usually twice per year, at a similar time each year, although the calls may vary due to operational timescale of the proton accelerator. It is strongly recommended to visit the facilities' websites prior to planning an experiment; links to the facility websites are available from muonsources. For all of these access panels, the proposals are peer reviewed and the highest rated proposals are taken forward for experiments. Proposals are usually short in duration, typically requesting a few days of beamtime, and may be from individual groups or a collaboration. Groups can, and often are, international. New users to the facilities are always welcome and considered favourably within each access panel.

Outlook

The future for muon spin spectroscopy is looking very encouraging. There are various strong developments, including new data analysis techniques, new instruments and new facilities. The current facilities are planning to remain in operation for the foreseeable future, and there are new facilities planned, including at the CSNS in China[179], RAON in South Korea[180] and the SNS in the USA[181].

Possible future sources and instruments

The EMuS facility at the CSNS will be a pulsed muon facility. However, unlike current pulsed facilities, the target for muon production will not be an intermediate target prior to a neutron target but will be a dedicated target taking the full proton beam into a long carbon target. To obtain the highest intensity of muons, a high field — 1 T for surface muons and 5 T for decay muons/pions — a capture solenoid is planned[182]. This will deliver either surface or decay muons to three experimental areas. Prior to this target, a thin target is envisaged for surface muon extraction. The time structure of the EMuS source is a repetition rate of 2.5 Hz, a pulse length of 50 ns and nominal power of 5 kW. It is intended that the initial spectrometer will have 128 detectors (64 forward and 64 backward); however, the next generation is being planned with 2,560 detectors[183]. This muon source will give a very high instantaneous data rate, which may be ideal for pulsed and in situ experiments.

The RAON facility is a new accelerator complex[184]. The main science goal of this new complex is the understanding of elements. This will result in a heavy ion accelerator. In addition, a muon spin spectroscopy facility is actively being considered. This would be a continuous muon source with a surface muon beamline, similar to those at PSI and TRIUMF.

The SNS muon facility is developing a laser extraction at the end of the linear accelerator[185]. This will neutralize the H^- ions, giving H^0. These will travel to the SNS linac dump and result in a 30 ns pulse at 50 kHz. This should enable a very high flux, which is optimized for the muon lifetime. It also allows for a muon source that does not require an intermediate target that can spoil the proton beam and enables the target to be fully optimized for muon production.

Instruments at existing muon facilities undergo constant small improvements to provide a better and broader range of science applications. However, there are regular, larger developments, such as major upgrades or new instruments. There are three major projects currently underway: FLAME (at PSI), Super-MuSR (at ISIS) and M9A/M9H (at TRIUMF). All of these instruments will significantly advance the muon technique and will be briefly summarized below.

The FLAME instrument at PSI will have a broad temperature (20 mK–310 K) and field (0–3 T) range, small samples (with virtually no background), an increased time resolution and a multistage sample holder for faster sample changes.

The Super-MuSR instrument at ISIS will have the addition of a muon pulse slicer to improve timing resolution at the pulse muon facility, greater number of detectors to improve positron count rates and a spin rotator for improved transverse field experiments[186].

M9A at TRIUMF is a surface muon beamline that will include a dedicated 3 T spectrometer equipped with APD (Avalanche Photo-Diode) detectors that will be optimized for rapid sample characterization with user-friendly operation. M9H will be a decay muon beamline with both longitudinal and transverse polarization. Its end station will have a configurable spectrometer that encompasses a dilution refrigerator and more conventional sample environments. Both longitudinal-field and transverse-field μSR measurements over wide ranges of magnetic fields (0–4 T), temperatures (40 mK–500 K) and pressures (up to 3 GPa) will be available within the set of sample environments being planned.

Future ISIS instrument plans include the improvement of an elemental analysis instrument, MuX, which should improve the counting rate by 10–1,000, and will be momentum and energy range-dependent.

Supercell
A large cell, generally associated with computation calculations, that is made up of many unit cells of the crystal structure.

This should be achieved by increased segmentation and will allow the full use of the incident muon flux.

PSI started a feasibility study to investigate the possibility of using state-of-the-art Si-Pixel detectors to determine the vertex of the muon decay with ≤1 mm precision. This vertex reconstruction will allow experiments to be performed at one order of magnitude higher beam rates, overcoming the pile-up problem at continuous muon sources, as demonstrated in a recent preprint article[187]. It will enable new research directions for μSR by much faster, higher statistics and more efficient measurements, measuring several samples simultaneously, introducing lateral spatial resolution and the option of applying external stimuli — pressure, light intensities, electric fields — at unprecedented levels due to sample sizes that can be reduced to <1 mm.

These new instruments and facilities are extremely important developments for the future of muon science and are the key enablers for future work and ideas, for example, reducing the size of samples required, needing more extreme environments, more complex set-ups or in situ experiments.

New techniques

DFT + μ. A problem that has challenged the μSR technique for many years is that although the magnetic field — from both nuclear and electronic magnetism — can be measured precisely at the muon site, the position of that site is not known a priori. There are various approaches that are being used to tackle this.

One of the most simple, the MUESR package, is based on using dipole–field and dipole–tensor sums using real space algorithms to solve the problem of the muon site[188]. The program is able to quickly and quantitatively solve the magnetic field at given muon sites. MUESR was able to reproduce the observed fields at four different stopping sites within the compound $CuSe_2O_5$ with good accuracy[189].

A more complex method is to use density functional theory, as has been demonstrated in two different cases. The first used a technique called DFT + μ, density functional theory with an included muon, where a calculation is performed of the total energy of a supercell of the structure to be modelled, but containing a muon located at a trial site[190,191]. The positions of the atoms in the supercell are then relaxed so that the muon can move and nearby ions distort[192]. If this is carried out with a large number of initial trial sites, and various schemes exist for efficiently sorting through the results[193], then the lowest energy site can be identified, as well as quantifying the associated muon-induced distortions[190,191].

The distortions induced by the muon can sometimes have rather dramatic consequences: one notable example is found in praseodymium-based pyrochlores in which the muon-induced distortion affects the crystal field level of the Pr^{3+} ions and splits a non-Kramers doublet ground state (FIG. 9). This allows the new singlet ground state to couple to the nuclear degrees of freedom, thereby producing a very large nuclear relaxation of the muon spin that dominates the muon response[194]. The DFT + μ technique has been applied to a wide range of materials, including inorganic[195] and molecular magnets[196],

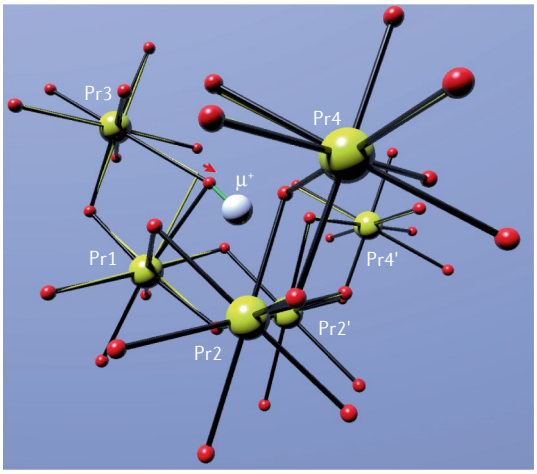

Fig. 9 | **The calculated muon site in $Pr_2Sn_2O_7$.** Local distortion induced by the presence of the muon. μ^+, positive muon. Adapted with permission from REF.[194], APS Physics.

as well as materials hosting skyrmion ground states[197]. In addition, the methods have been extended to consider hyperfine fields in metals[198] and quantum effects[199] associated with the muon site that can be important due to the muon's small mass.

The other density functional theory-based technique uses an Ab Initio Random Structure Searching (AIRSS) to locate the muon[200]. The approach relies on providing information on the crystal structure of the system, and through a series of random structure generation, the muon stopping sites can be solved. This approach was extended to organic-based samples where muonium interactions dominate, using density functional tight binding, although this is not a true ab initio technique. The approach was able to show agreement with previously observed results from the organic molecules; durene, TCNQ and bithiophene. Finally, the pymuon suite[201] uses an approach known as unperturbed electrostatic potential, working mainly for muons within a diamagnetic environment. This approach uses a distribution of ions, with a positively charged nuclei and negatively charged electronic cloud, to compute the Coulomb potential at the muon site. This points to the interaction of the muon with the surrounding atoms to be a chemical problem that can be applied to a host of different systems.

In summary, muon spin relaxation and rotation is an extremely powerful technique that yields useful and unique information to greatly enhance the understanding of topical and interesting materials. This Primer on muon spin spectroscopy has provided an overview of the broad science programme undertaken at muon facilities around the world. It is intended as a general introduction to the technique and highlights some of the successes that muon spin spectroscopy has had over the years. Recently, there have been numerous excellent textbooks published, or at the time of writing this Primer about to be published, that give more detailed information should it be required[6,8,13].

Published online: 27 January 2022

1. Anderson, C. D. & Neddermeyer, S. H. Cloud chamber observations of cosmic rays at 4300 meters elevation and near sea-level. *Phys. Rev.* **50**, 263–271 (1936).
2. Wulf, T. Über den Ursprung der in der Atmosphäre vorhandenen γ-Strahlung [German]. *Phys. Z.* **10**, 811 (1909).
3. Hess, V. F. Über Beobachtungen der durchdringenden Strahlung bei sieben Freiballonfahrten [German]. *Phys. Z.* **13**, 1084 (1912).
4. Garwin, R. L., Lederman, L. M. & Weinrich, M. Observations of the failure of conservation of parity and charge conjugation in meson decays — magnetic moment of the free muon. *Phys. Rev.* **105**, 1415–1417 (1957).
5. Conversi, M., Pancini, E. & Piccioni, O. On the decay process of positive and negative mesons. *Phys. Rev.* **68**, 232 (1945).
6. Blundell, S., De Renzi, R., Lancaster, T. & Pratt, F. *Introduction to Muon Spectroscopy* (Oxford Univ. Press, 2021).
7. Schenck, A. *Muon Spin Rotation: Principles and Applications in Solid State Physics* (Adam Hilger, 1985).
8. Yaouanc, A. & Dalmas de Réotier, P. *Muon Spin Rotation, Relaxation, and Resonance* (Oxford Univ. Press, 2010).
9. Nagamine, K. *Introductory Muon Science* (Cambridge Univ. Press, 2003).
10. Roduner, E. *The Positive Muon as a Probe in Free Radical Chemistry* (Springer, 1988).
11. Lee, S. L., Kilcoyne, S. H. & Cywinski, R. *Muon Science: Muons in Physics, Chemistry and Materials: Proceedings of the Fifty First Scottish Universities Summer School in Physics, St Andrews, August 1998* (Scottish Univ. Summer School in Physics, 1999).
12. Walker, D. C. *Muon and Muonium Chemistry* (Cambridge Univ. Press, 1983).
13. Morenzoni, E. & Amato, A. in *Lecture Notes in Physics* (Springer, 2022).
14. Matsuzaki, T. et al. The RIKEN-RAL pulsed muon facility. *Nucl. Instrum. Methods Phys. Res. A Accel. Spectrom. Detect. Assoc. Equip.* **465**, 365–383 (2001).
15. Hillier, A. D., Lord, J. S., Ishida, K. & Rogers, C. Muons at ISIS. *Philos. Trans. R. Soc. A Mathem. Phys. Eng. Sci.* **377**, 7 (2019).
16. Cook, S. et al. Delivering the world's most intense muon beam. *Phys. Rev. Accel. Beams* **20**, 030101 (2017).
17. Miyake, Y. et al. J-PARC muon facility, MUSE. *Phys. Procedia* **30**, 46–49 (2012).
18. Hillier, A. D. et al. Developments at the ISIS muon source and the concomitant benefit to the user community. *J. Phys. Conf. Ser.* **551**, 012067 (2014).
19. Giblin, S. R. et al. Optimising a muon spectrometer for measurements at the ISIS pulsed muon source. *Nucl. Instrum. Methods Phys. Res. A Accel. Spectrom. Detect. Assoc. Equip.* **751**, 70–78 (2014).
20. Abela, R. et al. Muons on request (MORE): combining advantages of continuous and pulsed muon beams. *Hyperfine Interact.* **120**, 575–578 (1999).
21. Bakule, P. & Morenzoni, E. Generation and applications of slow polarized muons. *Contemp. Phys.* **45**, 203–225 (2004).
This work demonstrates low-energy muons.
22. Khasanov, R. et al. High pressure research using muons at the Paul Scherrer Institute. *High. Press. Res.* **36**, 140–166 (2016).
23. Watanabe, I. et al. Development of a gas-pressurized high-pressure μSR setup at the RIKEN-RAL Muon Facility. *Phys. B Condens. Matter* **404**, 993–995 (2009).
24. Hillier, A. D., Cottrell, S. P., King, P. J. C., Eaton, G. H. & Clarke-Gayther, M. A. High frequency measurements at a pulsed muon source: beating the pulse width! *Phys. B-Condens. Matter* **326**, 275–278 (2003).
25. Cottrell, S. P., Johnson, C., Cox, S. F. J. & Scott, C. A. Radio-frequency techniques for muon charge state conversion measurements. *Phys. B Condens. Matter* **326**, 248–251 (2003).
26. Fleming, D. G., Cottrell, S. P., McKenzie, I. & Ghandi, K. Rate constants for the slow Mu plus propane abstraction reaction at 300 K by diamagnetic RF resonance. *Phys. Chem. Chem. Phys.* **17**, 19901–19910 (2015).
27. Kadono, R., Matsushita, A., Macrae, R. M., Nishiyama, K. & Nagamine, K. Muonium centers in crystalline Si and Ge under illumination. *Phys. Rev. Lett.* **73**, 2724–2727 (1994).
28. Yokoyama, K. et al. The new high field photoexcitation muon spectrometer at the ISIS pulsed neutron and muon source. *Rev. Sci. Instrum.* **87**, 12511 (2016).
29. Proksch, T., Chow, K. H., Salman, Z., Stilp, E. & Suter, A. Direct observation of hole carrier-density profiles and their light-induced manipulation at the surface of Ge. *Phys. Rev. Appl.* **14**, 014098 (2020).
30. Eshchenko, D. G., Storchak, V. G., Cottrell, S. P. & Morenzoni, E. Electric-field-enhanced neutralization of deep centers in GaAs. *Phys. Rev. Lett.* **103**, 216601 (2009).
31. Hillier, A. D., Paul, D. M. & Ishida, K. Probing beneath the surface without a scratch bulk non-destructive elemental analysis using negative muons. *Microchem. J.* **125**, 203–207 (2016).
32. Clemenza, M. et al. Muonic atom X-ray spectroscopy for non-destructive analysis of archeological samples. *J. Radioanal. Nucl. Chem.* **322**, 1357–1363 (2019).
33. Hillier, A., Seller, K. I. P., Veale, M. C. & Wilson, M. D. Element specific imaging using muonic X-rays. *JPS Conf. Proc.* **21**, 011042 (2018).
34. Yabu, G. et al. Imaging of muonic X-ray of light elements with a CdTe double-sided strip detector. *JPS Conf. Ser.* **21**, 011044 (2018).
35. Hayano, R. S. et al. Zero-and low-field spin relaxation studied by positive muons. *Phys. Rev. B* **20**, 850–859 (1979).
This work presents a comprehensive but concise and still actual description of the relaxations in zero and transverse fields. The principle of the techniques and the standard relaxation function are introduced.
36. Rainford, B. D. & Daniell, G. J. μ-SR frequency-spectra using the maximum-entropy method. *Hyperfine Interact.* **87**, 1129–1134 (1994).
37. McKenzie, I. The positive muon and μSR spectroscopy: powerful tools for investigating the structure and dynamics of free radicals and spin probes in complex systems. *Annu. Rep. Sect. C* **109**, 65–112 (2013).
38. Heming, M. et al. Detection of muonated free-radicals through the effects of avoided level-crossing — theory and analysis of spectra. *Chem. Phys. Lett.* **128**, 100–106 (1986).
39. Percival, P. W. et al. C-13 hyperfine coupling-constants in μC_{60}. *Chem. Phys. Lett.* **245**, 90–94 (1995).
40. Roduner, E., Reid, I. D., Ricco, M. & De Renzi, R. Anisotropy of 2-norbornyl radical reorientational dynamics in the plastic phase of norbornene as determined by ALC-μ-SR. *Ber. Bunsen Ges. Phys. Chem. Chem. Phys.* **93**, 1194–1197 (1989).
41. McKenzie, I., Scheuermann, R. & Sedlak, K. How do strain and steric interactions affect the reactions of aromatic compounds with free radicals? Characterization of the radicals formed by muonium addition to *p*-xylene and 2.2 paracyclophane by DFT calculations and muon spin spectroscopy. *J. Phys. Chem. A* **116**, 7765–7772 (2012).
42. Measday, D. F. The nuclear physics of muon capture. *Phys. Reports Rev. Sect. Phys. Lett.* **354**, 243–409 (2001).
43. Ninomiya, K., Kubo, M., Strasser, P., Shinohara, A., Tampo, M., Kawamura, N. & Miyake, Y. Isotope identification of lead by muon induced X-ray and γ-ray measurements. *JPS Conf. Proc.* **21**, 011043 (2018).
44. Suter, A. & Wojek, B. M. MuSRFit: a free platform-independent framework for mu SR data analysis. *12th Int. Conf. MuSpin Rotation Relax. Reson.* **30**, 69–73 (2012).
45. Pratt, F. L. WiMDA: a muon data analysis program for the Windows PC. *Phys. B* **289**, 710–714 (2000).
46. Baker, P. J., Loe, T., Telling, M., Cottrell, S. P. & Hillier, A. D. in *Proc. 14th Int. Conf. Muon Spin Rotation, Relaxation and Resonance (μSR2017)* Vol. 21 *JPS Conference Proceedings* (Physical Society of Japan, 2018).
47. Luetkens, H. et al. The electronic phase diagram of the $LaO_{1-x}F_xFeAs$ superconductor. *Nat. Mater.* **8**, 305–309 (2009).
48. Drew, A. J. et al. Coexistence of static magnetism and superconductivity in $SmFeAsO_{1-x}F_x$ as revealed by muon spin rotation. *Nat. Mater.* **8**, 310–314 (2009).
49. Parker, D. R. et al. Control of the competition between a magnetic phase and a superconducting phase in cobalt-doped and nickel-doped NaFeAs using electron count. *Phys. Rev. Lett.* **104**, 057007 (2010).
50. Hayward, M. A. et al. The hydride anion in an extended transition metal oxide array: $LaSrCoO_3H_{0.7}$. *Science* **295**, 1882–1884 (2002).
51. Campbell, I. A. et al. Dynamics in canonical spin-glasses observed by muon spin depolarization. *Phys. Rev. Lett.* **72**, 1291–1294 (1994).
52. Lovesey, S. W., Trohidou, K. N. & Karlsson, E. B. Muon spin relaxation in ferromagnets. 2. Critical and paramagnetic magnetization fluctuations. *J. Phys. Condens. Matter* **4**, 2061–2071 (1992).
53. Uemura, Y. J. et al. Phase separation and suppression of critical dynamics at quantum phase transitions of MnSi and $(Sr_{1-x}Ca_x)RuO_3$. *Nat. Phys.* **3**, 29–35 (2007).
54. Uemura, Y. J., Harshman, D. R., Senba, M., Ansaldo, E. J. & Murani, A. P. Zero-field muon-spin relaxation in CuMn spin-glasses compared with neutron and susceptibility experiments. *Phys. Rev. B* **30**, 1606–1608 (1984).
55. Yaouanc, A., Dereotier, P. D. & Frey, E. Zero-field muon-spin-relaxation depolarization rate of paramagnets near the Curie-temperature. *Phys. Rev. B* **47**, 796–809 (1993).
56. Pratt, F. et al. Muon spin relaxation studies of critical fluctuations and diffusive spin dynamics in molecular magnets. *Phys. B: Condens. Matter* **404**, 585–589 (2009).
57. Berlie, A., Terry, I. & Szablewski, M. A 3D antiferromagnetic ground state in a quasi-1D π-stacked charge-transfer system. *J. Mater. Chem. C.* **6**, 12468–12472 (2018).
58. Adroja, D. T. et al. Muon spin rotation and neutron scattering investigations of the B-site ordered double perovskite Sr_2DyRuO_6. *Phys. Rev. B* **101**, 13 (2020).
59. Yamauchi, H. et al. High-temperature short-range order in Mn_3RhSi. *Commun. Mater.* **1**, 43 (2020).
60. Dally, R. et al. Short-range correlations in the magnetic ground state of $Na_4Ir_3O_8$. *Phys. Rev. Lett.* **113**, 247601 (2014).
61. Rainford, B. D., Cywinski, R. & Dakin, S. J. Neutron and μ-SR studies of spin fluctuations in YMn_2 and related alloys. *J. Magn. Magn. Mater.* **140**, 805–806 (1995).
62. Le, L. P. et al. Searching for spontaneous magnetic order in an organic ferromagnet — μ-SR studies of β-phase p-NPNN. *Chem. Phys. Lett.* **206**, 405–408 (1993).
63. Blundell, S. J. et al. μ^+ SR of the organic ferromagnet p-NPNN — diamagnetic and paramagnetic states. *Europhys. Lett.* **31**, 573–578 (1995).
64. Kojima, K. M. et al. Reduction of ordered moment and Neel temperature of quasi-one-dimensional antiferromagnets Sr_2CuO_3 and Ca_2CuO_3. *Phys. Rev. Lett.* **78**, 1787–1790 (1997).
65. Sengupta, P., Sandvik, A. W. & Singh, R. R. P. Specific heat of quasi-two-dimensional antiferromagnetic Heisenberg models with varying interplanar couplings. *Phys. Rev. B* **68**, 7 (2003).
66. Lancaster, T. et al. Magnetic order in the quasi-one-dimensional spin-1/2 molecular chain compound copper pyrazine dinitrate. *Phys. Rev. B* **73**, 020410 (2006).
67. Pratt, F. L., Blundell, S. J., Lancaster, T., Baines, C. & Takagi, S. Low-temperature spin diffusion in a highly ideal $S = 1/2$ Heisenberg antiferromagnetic chain studied by muon spin relaxation. *Phys. Rev. Lett.* **96**, 247203 (2006).
68. Manson, J. L. et al. $Ag(nic)_2$ (nic=nicotinate): a spin-canted quasi-2D antiferromagnet composed of square-planar $S = 1/2$ Ag-II ions. *Inorg. Chem.* **51**, 1989–1991 (2012).
69. Lancaster, T. et al. Quantum magnetism in molecular spin ladders probed with muonspin spectroscopy. *New. J. Phys.* **20**, 103002 (2018).
70. Pratt, F. Superconductivity and magnetism in organic materials studied with μSR. *J. Phys. Soc. Jpn.* **85**, 091008 (2016).
71. Amato, A. et al. Understanding the μSR spectra of MnSi without magnetic polarons. *Phys. Rev. B* **89**, 184425 (2014).
72. Wang, R. Z. et al. Quantum griffiths phase inside the ferromagnetic phase of $Ni_{1-x}V_x$. *Phys. Rev. Lett.* **118**, 267202 (2017).
73. Frandsen, B. A. et al. Volume-wise destruction of the antiferromagnetic Mott insulating state through quantum tuning. *Nat. Commun.* **7**, 12519 (2016).
74. Kirschner, F. K. K. et al. Spin Jahn–Teller antiferromagnetism in $CoTi_2O_5$. *Phys. Rev. B* **99**, 064403 (2019).
75. Pratt, F. L. et al. Magnetic and non-magnetic phases of a quantum spin liquid. *Nature* **471**, 612–616 (2011).
76. Yaouanc, A. et al. Dynamical splayed ferromagnetic ground state in the quantum spin ice $Yb_2Sn_2O_7$. *Phys. Rev. Lett.* **110**, 127207 (2013).
77. Kirschner, F. K. K., Flicker, F., Yacoby, A., Yao, N. Y. & Blundell, S. J. Proposal for the detection of magnetic monopoles in spin ice via nanoscale magnetometry. *Phys. Rev. B* **97**, 140402(R) (2018).
78. Brewer, J. H. et al. Observation of muon–fluorine hydrogen-bonding in ionic-crystals. *Phys. Rev. B* **33**, 7813–7816 (1986).

79. Lancaster, T. et al. Muon–fluorine entangled states in molecular magnets. *Phys. Rev. Lett.* **99**, 267601 (2007).
80. Wilkinson, J. M. & Blundell, S. J. Information and decoherence in a muon–fluorine coupled system. *Phys. Rev. Lett.* **125**, 087201 (2020).
This work demonstrates the use of muons to model fundamental decoherence effects in the solid state.
81. Aidoudi, F. H. et al. An ionothermally prepared $S=1/2$ vanadium oxyfluoride kagome lattice. *Nat. Chem.* **3**, 801–806 (2011).
82. Abdeldaim, A. H. et al. Realizing square and diamond lattice $S=1/2$ Heisenberg antiferromagnet models in the α and β phases of the coordination framework, $KTi(C_2O_4)_2 \cdot xH_2O$. *Phys. Rev. Mater.* **4**, 104414 (2020).
83. Mendels, P. et al. Quantum magnetism in the paratacamite family: towards an ideal kagome lattice. *Phys. Rev. Lett.* **98**, 077204 (2007).
This work shows that μSR has an unparalleled sensitivity to magnetic fields. This specificity is used in this article to discard even weak magnetic freezing in the first kagome-based quantum spin liquid candidate.
84. Majumder, M. et al. Breakdown of magnetic order in the pressurized kitaev iridate β-Li_2IrO_3. *Phys. Rev. Lett.* **120**, 237202–237202 (2018).
85. Li, Y. et al. Muon spin relaxation evidence for the U_1 quantum spin-liquid ground state in the triangular antiferromagnet $YbMgGaO_4$. *Phys. Rev. Lett.* **117**, 97201–97201 (2016).
86. Colman, R. H. et al. Spin dynamics in the $S=1/2$ quantum kagome compound vesignieite, $Cu_3Ba(VO_5H)_2$. *Phys. Rev. B* **83**, 180416 (2011).
87. Pratt, F. L. Probing quantum critical spin liquids with μSR. *JPS Conf. Proc.* **21**, 011002 (2018).
88. Gomilšek, M. et al. Kondo screening in a charge-insulating spinon metal. *Nat. Phys.* **15**, 754–758 (2019).
89. Amato, A. Heavy-fermion systems studied by μSR technique. *Rev. Mod. Phys.* **69**, 1119–1179 (1997).
This work reviews the impact muons have had in the field of heavy fermion science.
90. Sonier, J. E., Brewer, J. H. & Kiefl, R. F. μSR studies of the vortex state in type-II superconductors. *Rev. Mod. Phys.* **72**, 769–811 (2000).
This work presents a superconductivity review on the impact of muons.
91. Tinkham, M. *Introduction to Superconductivity* 2nd edn (McGraw Hill, 1996).
92. Sonier, J. E. μSR studies of cuprate superconductors. *J. Phys. Soc. Jpn.* **85**, 091005 (2016).
93. Khasanov, R. et al. Two-gap superconductivity in $Ba_{1-x}K_xFe_2As_2$: a complementary study of the magnetic penetration depth by muon-spin rotation and angle-resolved photoemission. *Phys. Rev. Lett.* **102**, 187005 (2009).
94. Uemura, Y. J. Dynamic superconductivity responses in photoexcited optical conductivity and Nernst effect. *Phys. Rev. Mater.* **3**, 104801 (2019).
95. Uemura, Y. J. et al. Magnetic-field penetration depth in $Tl_2Ba_2CuO_{6+\delta}$ in the overdoped regime. *Nature* **364**, 605–607 (1993).
96. Sigrist, M. & Ueda, K. Phenomenological theory of unconventional superconductivity. *Rev. Mod. Phys.* **63**, 239–311 (1991).
97. Schenck, A. in *Muon Science: Muons in Physics, Chemistry and Materials.Muon Science: Muons in Physics, Chemistry and Materials* (eds Lee, S. L., Cywinski, R. & Kilcoyne, S. H.) 39–84 (Institute of Physics, 1999).
98. Luke, G. M. et al. Time-reversal symmetry breaking superconductivity in Sr_2RuO_4. *Nature* **394**, 558–561 (1998).
99. Hillier, A. D., Quintanilla, J. & Cywinski, R. Evidence for time-reversal symmetry breaking in the noncentrosymmetric superconductor $LaNiC_2$. *Phys. Rev. Lett.* **102**, 117007 (2010).
100. Aoki, Y. et al. Time-reversal symmetry-breaking superconductivity in heavy-fermion $PrOs_4Sb_{12}$ detected by muon-spin relaxation. *Phys. Rev. Lett.* **91**, 067003 (2003).
101. Maisuradze, A. et al. Evidence for time-reversal symmetry breaking in superconducting $PrPt_4Ge_{12}$. *Phys. Rev. B* **82**, 024524 (2010).
102. Ghosh, S. K. et al. Recent progress on superconductors with time-reversal symmetry breaking. *J. Phys. Condens. Matter* **33**, 28 (2021).
This recent review on TRS breaking shows the impact of muon experiments in the discovery and understanding of unconventional superconductors.
103. Adachi, T. et al. Muon spin relaxation and magnetic susceptibility studies of the effects of nonmagnetic impurities on the Cu spin dynamics and superconductivity in $La_{2-x}Sr_xCu_{1-y}Zn_yO_4$ around $x=0.115$. *Phys. Rev. B* **69**, 184507 (2004).
104. Zhang, J. et al. Discovery of slow magnetic fluctuations and critical slowing down in the pseudogap phase of $YBa_2Cu_3O_y$. *Sci. Adv.* **4**, eaao5235 (2018).
105. Kaiser, C. T. et al. Li mobility in the battery cathode material $Li_x[Mn_{1.96}LiO.O_4]O_4$ studied by muon-spin relaxation. *Phys. Rev. B* **62**, R9236–R9239 (2000).
106. Ariza, M. J., Jones, D. J., Roziere, J., Lord, J. S. & Ravot, D. Muon spin relaxation study of spinel lithium manganese oxides. *J. Phys. Chem. B* **107**, 6003–6011 (2003).
107. Sugiyama, J. et al. Li diffusion in Li_xCoO_2 probed by muon-spin spectroscopy. *Phys. Rev. Lett.* **103**, 147601 (2009).
This significant paper shows lithium diffusion observed by μSR and opens the field of the application of energy materials to μSR.
108. Medarde, M. et al. 1D to 2D Na^+ ion diffusion inherently linked to structural transitions in $Na_{0.7}CoO_2$. *Phys. Rev. Lett.* **110**, 266401 (2013).
109. Mansson, M. & Sugiyama, J. Muon-spin relaxation study on Li- and Na-diffusion in solids. *Phys. Scr.* **88**, 068509 (2013).
110. Sugiyama, J. et al. Lithium diffusion in $LiMnPO_4$ detected with μ^+-SR. *Phys. Rev. Res.* **2**, 033161 (2020).
111. Kadono, R. et al. Hydrogen bonding in sodium alanate: a muon spin rotation study. *Phys. Rev. Lett.* **100**, 026401 (2008).
112. Sugiyama, J. et al. Desorption reaction in MgH_2 studied with in situ μ^+SR. *Sustain. Energ. Fuels* **3**, 956–964 (2019).
113. Sugiyama, J. et al. Nuclear magnetic field in solids detected with negative-muon spin rotation and relaxation. *Phys. Rev. Lett.* **121**, 087202 (2018).
114. Roduner, E. et al. Quantum phenomena and solvent effects on addition of hydrogen isotopes to benzene and to dimethylbutadiene. *Ber. Bunsen Ges. Phys. Chem. Chem. Phys.* **94**, 1224–1230 (1990).
115. Nicovich, J. M. & Ravishankara, A. R. Reaction of hydrogen-atom with benzene — kinetics and mechanism. *J. Phys. Chem.* **88**, 2534–2541 (1984).
116. Mezyk, S. P. & Bartels, D. M. Rate-constant and activation-energy measurement for the reaction of atomic-hydrogen with methanol, iodomethane, iodoethane, and 1-iodopropane in aqueous-solution. *J. Phys. Chem.* **98**, 10578–10583 (1994).
117. Ghandi, K. et al. Muonium kinetics in sub- and supercritical water. *Phys. B Condens. Matter* **326**, 55–60 (2003).
118. Percival, P. W., Brodovitch, J. C., Ghandi, K., McCollum, B. M. & McKenzie, I. H atom kinetics in superheated water studied by muon spin spectroscopy. *Radiat. Phys. Chem.* **76**, 1231–1235 (2007).
119. Laidler, K. J. & Keith, J. *Chemical Kinetics* (Harper & Row, 1987).
120. Chandrasena, L. et al. Free radical reactivity of a phosphaalkene explored through studies of radical isotopologues. *Angew. Chem. Int. Ed.* **58**, 297–301 (2019).
121. Veatch, S. L., Leung, S. S. W., Hancock, R. E. W. & Thewalt, J. L. Fluorescent probes alter miscibility phase boundaries in ternary vesicles. *J. Phys. Chem. B* **111**, 502–504 (2007).
122. Hamley, I. W. *Introduction to Soft Matter: Synthetic and Biological Self-Assembling Materials, Revised Edition* (Wiley, 2007).
123. Safinya, C. R., Sirota, E. B., Roux, D. & Smith, G. S. Universality in interacting membranes — the effect of cosurfactants on the interfacial rigidity. *Phys. Rev. Lett.* **62**, 1134–1137 (1989).
124. Roduner, E. Muons, soap, and drug delivery — an invitation to enter a new field of research. *Phys. B Condens. Matter* **326**, 19–24 (2003).
This work demonstrates the potential advances for ALC-μSR.
125. Scheuermann, R. et al. Partitioning of small amphiphiles at surfactant bilayer/water interfaces: an avoided level crossing muon spin resonance study. *Langmuir* **20**, 2652–2659 (2004).
126. Kiefl, R. F. et al. ^{29}Si hyperfine structure of anomalous muonium in silicon: proof of the bond-centered model. *Phys. Rev. Lett.* **60**, 224–226 (1988).
127. Cox, S. F. J. et al. Experimental confirmation of the predicted shallow donor hydrogen state in zinc oxide. *Phys. Rev. Lett.* **86**, 2601–2604 (2001).
This work describes the pioneer contribution of μSR to the understanding of the role of hydrogen in semiconductors, namely when it incorporates the lattice structure either in a bond-centre configuration or as a shallow donor.
128. Hofmann, D. M. et al. Hydrogen: a relevant shallow donor in zinc oxide. *Phys. Rev. Lett.* **88**, 045504 (2002).
129. Vilão, R. C. et al. Muonium donor in rutile TiO_2 and comparison with hydrogen. *Phys. Rev. B* **92**, 081202 (2015).
130. Brant, A. T., Yang, S., Giles, N. C. & Halliburton, L. E. Hydrogen donors and Ti^{3+} ions in reduced TiO_2 crystals. *J. Appl. Phys.* **110**, 053714 (2011).
131. Gorelkinskii, Y. V. in *Hydrogen in Semiconductors II (Volume 61) Semiconductors and Semimetals* Ch. 3 (ed. Nickel, N. H.) 25–77 (Academic Press, 1999).
132. Cox, S. F. J. Muonium as a model for interstitial hydrogen in the semiconducting and semimetallic elements. *Rep. Prog. Phys.* **72**, 116501 (2009).
133. Gil, J. M. et al. Novel muonium state in CdS. *Phys. Rev. Lett.* **83**, 5294–5297 (1999).
134. Yokoyama, K., Lord, J. S., Miao, J., Murahari, P. & Drew, A. J. Photoexcited muon spin spectroscopy: a new method for measuring excess carrier lifetime in bulk silicon. *Phys. Rev. Lett.* **119**, 226601 (2017).
135. Alberto, H. V. et al. Slow-muon study of quaternary solar-cell materials: single layers and p–n junctions. *Phys. Rev. Mater.* **2**, 025402 (2018).
136. Woerle, J., Prokscha, T., Hallēn, A. & Grossner, U. Interaction of low-energy muons with defect profiles in proton-irradiated Si and 4H-SiC. *Phys. Rev. B* **100**, 115202 (2019).
137. Jackson, T. J. et al. Depth-resolved profile of the magnetic field beneath the surface of a superconductor with a few nm resolution. *Phys. Rev. Lett.* **84**, 4958–4961 (2000).
138. Suter, A. et al. Observation of nonexponential magnetic penetration profiles in the Meissner state: a manifestation of nonlocal effects in superconductors. *Phys. Rev. B* **72**, 024506 (2005).
139. Kozhevnikov, V. et al. Nonlocal effect and dimensions of Cooper pairs measured by low-energy muons and polarized neutrons in type-I superconductors. *Phys. Rev. B* **87**, 104508 (2013).
140. Stilp, E. et al. Controlling the near-surface superfluid density in underdoped $YBa_2Cu_3O_{6+x}$ by photo-illumination. *Sci. Rep.* **4**, 6250 (2014).
141. Kozhevnikov, V., Suter, A., Prokscha, T. & Van Haesendonck, C. Experimental study of the magnetic field distribution and shape of domains near the surface of a type-I superconductor in the iIntermediate state. *J. Supercond. Nov. Magn.* **33**, 3361–3376 (2020).
142. Morenzoni, E. et al. The Meissner effect in a strongly underdoped cuprate above its critical temperature. *Nat. Commun.* **2**, 272 (2011).
143. Di Bernardo, A. et al. Intrinsic paramagnetic meissner effect due to s-wave odd-frequency superconductivity. *Phys. Rev. X* **5**, 041021 (2015).
144. Flokstra, M. G. et al. Remotely induced magnetism in a normal metal using a superconducting spin-valve. *Nat. Phys.* **12**, 57–61 (2016).
145. Flokstra, M. G. et al. Observation of anomalous meissner screening in Cu/Nb and Cu/Nb/Co thin films. *Phys. Rev. Lett.* **120**, 247001 (2018).
146. Stewart, R. et al. Controlling the electromagnetic proximity effect by tuning the mixing between superconducting and ferromagnetic order. *Phys. Rev. B* **100**, 020505(R) (2019).
147. Krieger, J. A. et al. Proximity-induced odd-frequency superconductivity in a topological insulator. *Phys. Rev. Lett.* **125**, 026802 (2020).
148. Boris, A. V. et al. Dimensionality control of electronic phase transitions in nickel-oxide superlattices. *Science* **332**, 937–940 (2011).
149. Suter, A. et al. Two-dimensional magnetic and superconducting phases in metal-insulator $La_{2-x}Sr_xCuO_4$ superlattices measured by muon-spin rotation. *Phys. Rev. Lett.* **106**, 237003 (2011).
150. Suter, A. et al. Superconductivity drives magnetism in δ-doped La_2CuO_4. *Phys. Rev. B* **97**, 134522 (2018).
151. Stilp, E. et al. Magnetic phase diagram of low-doped $La_{2-x}Sr_xCuO_4$ thin films studied by low-energy muon-spin rotation. *Phys. Rev. B* **88**, 064419 (2013).
152. Maurel, L. et al. Nature of antiferromagnetic order in epitaxially strained multiferroic $SrMnO_3$ thin films. *Phys. Rev. B* **92**, 024419 (2015).
153. Langenberg, E. et al. Controlling the electrical and magnetoelectric properties of epitaxially strained $Sr_{1-x}Ba_xMnO_3$ thin films. *Adv. Mater. Interfaces* **4**, 1601040 (2017).

154. Maurel, L. et al. Engineering the magnetic order in epitaxially strained $Sr_{1-x}Ba_xMnO_3$ perovskite thin films. *APL. Mater.* **7**, 041117 (2019).
155. Dunsiger, S. R. et al. Spatially homogeneous ferromagnetism of (Ga, Mn)As. *Nat. Mater.* **9**, 299–303 (2010).
156. Monteiro, P. M. S. et al. Spatially homogeneous ferromagnetism below the enhanced curie temperature in EuO_{1-x} thin films. *Phys. Rev. Lett.* **110**, 217208 (2013).
157. Saadaoui, H. et al. Intrinsic ferromagnetism in the diluted magnetic semiconductor Co:TiO_2. *Phys. Rev. Lett.* **117**, 227202 (2016).
158. Levchenko, K. et al. Evidence for the homogeneous ferromagnetic phase in (Ga, Mn) (Bi, As) epitaxial layers from muon spin relaxation spectroscopy. *Sci. Rep.* **9**, 3394 (2019).
159. Drew, A. J. et al. Direct measurement of the electronic spin diffusion length in a fully functional organic spin valve by low-energy muon spin rotation. *Nat. Mater.* **8**, 109–114 (2009).
160. Al Ma'Mari, F. et al. Beating the Stoner criterion using molecular interfaces. *Nature* **524**, 69 (2015).
161. Moorsom, T. et al. Reversible spin storage in metal oxide–fullerene heterojunctions. *Sci. Adv.* **6**, aax1085 (2020).
162. Hofmann, A. et al. Depth-dependent spin dynamics in thin films of $TbPc_2$ nanomagnets explored by low-energy implanted muons. *ACS Nano* **6**, 8390–8396 (2012).
163. Kiefl, E. et al. Robust magnetic properties of a sublimable single-molecule magnet. *ACS Nano* **10**, 5663–5669 (2016).
164. Prokscha, T. et al. Depth dependence of the ionization energy of shallow hydrogen states in ZnO and CdS. *Phys. Rev. B* **90**, 235303 (2014).
165. Hampshire, B. V. et al. Using negative muons as a probe for depth profiling silver roman coinage. *Heritage* **2**, 400–407 (2019).
166. Ponting, K. B. M. *The Metallurgy of Roman Silver Coinage: From the Reform of Nero to the Reform of Trajan* (Cambridge Univ. Press, 2015).
167. Moreno-Suarez, A. I. et al. First attempt to obtain the bulk composition of ancient silver–copper coins by using XRF and GRT. *Nucl. Instrum. Methods Phys. Res. Sect. B Beam Interact. Mater. At.* **358**, 93–97 (2015).
168. Green, G. Understanding roman gold coinage inside out. *J. Archaeol. Sci.* **134**, 105470 (2021).
169. Ninomiya, K. et al. Nondestructive elemental depth-profiling analysis by muonic X-ray measurement. *Anal. Chem.* **87**, 4597–4600 (2015).
170. Clemenza, M. et al. CHNET-TANDEM experiment: use of negative muons at RIKEN-RAL Port4 for elemental characterization of "Nuragic votive ship" samples. *Nucl. Instrum. Methods Phys. Res. Sect. A Accel. Spectrom.Detect. Assoc. Equip.* **936**, 27–28 (2019).
171. Kohler, E., Bergmann, R., Daniel, H., Ehrhart, P. & Hartmann, F. J. Application of muonic X-ray techniques to the elemental analysis of archaeological objects. *Nucl. Instrum. Methods Phys. Res.* **187**, 563–568 (1981).
172. Reidy, J. J., Hutson, R. L., Daniel, H. & Springer, K. Use of muonic X rays for nondestructive analysis of bulk samples of low *Z* constituents. *Anal. Chem.* **50**, 40–44 (1978).
173. Reidy, J. J., Hutson, R. L. & Springer, K. Use of muonic X rays for tissue analysis. *IEEE TAmuactionz NbuCteak Sci.* **NS-22**, 1780–1783 (1975).
174. Hillier, A. D., Hampshire, B. V. & Ishida, K. in *Handbook of Cultural Heritage Analysis* (eds D'Amico S. & Venuti, V.) (Springer, 2020).
175. Ziegler, J. F. & Lanford, W. A. Effect of cosmic-rays on computer memories. *Science* **206**, 776–788 (1979).
176. Sierawski, B. D. et al. Bias dependence of muon-induced single event upsets in 28 nm static random access memories. *2014 IEEE Int. Reliability Physics Symp.* https://doi.org/10.1109/IRPS.2014.6860585 (2014).
177. Sierawski, B. D. et al. Muon-induced single event upsets in deep-submicron technology. *IEEE Trans. Nucl. Sci.* **57**, 3273–3278 (2010).
178. Mahara, T. et al. Irradiation test of 65-nm bulk SRAMs with DC muon beam at RCNP-MuSIC Facility. *IEEE Trans. Nucl. Sci.* **67**, 1555–1559 (2020).
179. Tang, J. Y. et al. EMuS muon facility and its application in the study of magnetism. *Quant. Beam Sci.* **2**, 23 (2018).
180. Won, E. A proposed muon facility in RAON/Korea. *JPS Conf. Proc.* **2**, 010110 (2014).
181. Williams, T. J. & MacDougall, P. G. J. *Future muon source possibilities at the SNS* (SNS, 2017).
182. Jing, H. T., Meng, C., Tang, J. Y., Ye, B. J. & Sun, J. L. Production target and muon collection studies for an experimental muon source at CSNS. *Nucl. Instrum. Methods Phys. Res. A Accel. Spectrom. Detect. Assoc. Equip.* **684**, 109–116 (2012).
183. Pan, Z. W. et al. Conceptual design and update of the 128-channel μSR prototype spectrometer based on musrSim. *JJAP Conf. Proc.* **7**, 011303 (2019).
184. Kim, Y. J. Current status of experimental facilities at RAON. *Nucl. Instrum. Methods Phys. Res. Sect. B Beam Interact. Mater. At.* **463**, 408–414 (2020).
185. Liu, Y., Rakhman, A., Long, C. D. & Williams, T. J. Laser-assisted high-energy proton pulse extraction for feasibility study of co-located muon source at the SNS. *Nucl. Instrum. Methods Phys. Res. A Accel. Spectrom. Detect. Assoc. Equip.* **962**, 163706 (2020).
186. Hillier, A. D. et al. in *Proc. 14th Int. Conf. Muon Spin Rotation, Relaxation and Resonance (μSR2017)* Vol. 21 *JPS Conference Proceedings* (The Physical Society of Japan, 2018).
187. Aiba, M. et al. Science case for the new high-intensity muon beams HIMB at PSI. Preprint at https://arxiv.org/abs/2111.05788 (2021).
188. Bonfà, P., Onuorah, I. J. & De Renzi, R. in *Proc. 14th Int. Conf. Muon Spin Rotation, Relaxation and Resonance (μSR2017)* Vol. 21 *JPS Conference Proceedings* (The Physical Society of Japan, 2018).
189. Herak, M. et al. Magnetic order and low-energy excitations in the quasi-one-dimensional antiferromagnet $CuSe_2O_5$ with staggered fields. *Phys. Rev. B* **87**, 104413 (2013).
190. Moller, J. S., Ceresoli, D., Lancaster, T., Marzari, N. & Blundell, S. J. Quantum states of muons in fluorides. *Phys. Rev. B* **87**, 121108 (2013).
191. Bernardini, F., Bonfa, P., Massidda, S. & De Renzi, R. Ab initio strategy for muon site assignment in wide band gap fluorides. *Phys. Rev. B* **87**, 115148 (2013).
192. Moller, J. S. et al. Playing quantum hide-and-seek with the muon: localizing muon stopping sites. *Phys. Scr.* **88**, 068510 (2013).
193. Bonfa, P. & De Renzi, R. Toward the computational prediction of muon sites and interaction parameters. *J. Phys. Soc. Jpn.* **85**, 10 (2016).
194. Foronda, F. R. et al. Anisotropic local modification of crystal field levels in Pr-based pyrochlores: a muon-induced effect modeled using density functional theory. *Phys. Rev. Lett.* **114**, 017602 (2015).
195. Bonfa, P., Sartori, F. & De Renzi, R. Efficient and reliable strategy for identifying muon sites based on the double adiabatic approximation. *J. Phys. Chem. C* **119**, 4278–4285 (2015).
196. Blundell, S. J. et al. μSR study of magnetic order in the organic quasi-one-dimensional ferromagnet F_4BImNN. *Phys. Rev. B* **88**, 064423 (2013).
197. Huddart, B. M. et al. Magnetic order and enhanced exchange in the quasi-one-dimensional molecule-based antiferromagnet $Cu(NO_3)_2(pyz)_3$. *Phys. Chem. Chem. Phys.* **21**, 1014–1018 (2019).
198. Franke, K. J. A. et al. Magnetic phases of skyrmion-hosting $GaV_4S_{8-y}Se_y$ ($y = 0, 2, 4, 8$) probed with muon spectroscopy. *Phys. Rev. B* **98**, 054428 (2018).
199. Onuorah, I. J., Bonfa, P. & De Renzi, R. Muon contact hyperfine field in metals: a DFT calculation. *Phys. Rev. B* **97**, 174414 (2018).
200. Liborio, L., Sturniolo, S. & Jochym, D. Computational prediction of muon stopping sites using ab initio random structure searching (AIRSS). *J. Chem. Phys.* **148**, 9 (2018).
201. Sturniolo, S. & Liborio, L. Computational prediction of muon stopping sites: a novel take on the unperturbed electrostatic potential method. *J. Chem. Phys.* **153**, 10 (2020).
202. Manson, J. L. et al. $Cu(HF_2)(pyz)_2BF_4$ (pyz = pyrazine): long-range magnetic ordering in a pseudo-cubic coordination polymer comprised of bridging HF_2- and pyrazine ligands. *Chem. Commun.* **2006**, 4894–4896 (2006).
203. Pant, A. D. et al. Characterization and optimization of ultra slow muon beam at J-PARC/MUSE: a simulation study. *Nucl. Instrum. Methods Phys. Res. A Accel. Spectrom. Detect. Assoc. Equip.* **929**, 129–133 (2019).
204. Nakamura, J. et al. Ultra slow muon microscope at MUSE/J-PARC. *J. Phys. Conf. Ser.* **502**, 012042 (2014).
205. Miyake, Y. et al. Ultra slow muon project at J-PARC MUSE. *J. Phys. Soc. Jpn.* **2**, 010101 (2014).
206. Prokscha, T. et al. The new μE4 beam at PSI: a hybrid-type large acceptance channel for the generation of a high intensity surface-muon beam. *Nucl. Instrum. Methods Phys. Res. A Accel. Spectrom. Detect. Assoc. Equip.* **595**, 317–331 (2008).
207. Morenzoni, E., Prokscha, T., Suter, A., Luetkens, H. & Khasanov, R. Nano-scale thin film investigations with slow polarized muons. *J. Phys. Condens. Matter* **16**, S4583–S4601 (2004).

Acknowledgements
All authors acknowledge the support and access of the muon facilities around the world. In particular, the staff scientists and technical support teams over the years. F.B. acknowledges the support of the French Agence Nationale de la Recherche, under Grant No. ANR-18-CE30-0022. I.M. acknowledges the support of a Discovery Grant from the Natural Sciences and Engineering Research Council of Canada. A.D.H. acknowledges the support of an ERC grant (RACOM). H.A. acknowledges funds from FEDER (Programa Operacional Factores de Competitividade COMPETE) and from FCT- Fundação para a Ciência e Tecnologia, I. P. (Portugal) under projects UIDB/04564/2020, UIDP/04564/2020 and PTDC/FIS-MAC/29696/2017. L.S. acknowledges support from the National Natural Science Foundations of China, No. 12174065, and the Shanghai Municipal Science and Technology No. 20ZR1405300.

Author contributions
Introduction (A.D.H.); Experimentation (A.B., K.S., I.M., T.P., I.W. and A.D.H.); Results (K.S., I.M. and A.D.H.); Applications (S.J.B., F.B., L.S., I.U., J.A.W., I.M., H.A., T.P., I.W. and A.D.H.); Reproducibility and data deposition (A.D.H.); Limitations and optimizations (A.D.H. and A.B.); Outlook (A.D.H., S.J.B. and T.P.); Overview of the Primer (A.D.H.). All authors reviewed the content of the primer.

Competing interests
The authors declare no competing interests.

Peer review information
Nature Reviews Methods Primers thanks Thomas Ashton, Pierre Dalmas de Reotier, Jingyu Tang and the other, anonymous, reviewer(s) for their contribution to the peer review of this work.

Publisher's note
Springer Nature remains neutral with regard to jurisdictional claims in published maps and institutional affiliations.

Supplementary information
The online version contains supplementary material available at https://doi.org/10.1038/s43586-021-00089-0.

RELATED LINKS
FLAME instrument: https://www.psi.ch/en/smus/flame-project
ISIS muons: https://www.isis.stfc.ac.uk/Pages/muons.aspx
J-PARC muons: https://j-parc.jp/researcher/MatLife/en/instrumentation/ms.html
Low-Energy Muons Group: https://www.psi.ch/en/low-energy-muons
Mantid: https://www.mantidproject.org/Main_Page
Muonsources: https://muonsources.org/
MuSIC: http://www.rcnp.osaka-u.ac.jp/RCNPhome/music/
NIST: http://physics.nist.gov/cuu/Constants/index.html
PSI: https://www.psi.ch/en/smus/instruments
PSI muons: https://www.psi.ch/en/lmu
Super-MuSR instrument: https://www.isis.stfc.ac.uk/Pages/Super-MuSR.aspx
TRIUMF: http://cmms.triumf.ca